Characterization and Modeling of filled rubber submitted to thermal aging

R. Bouaziz, K.D. Ahose, S. Lejeunes, D. Eyheramendy, F. Sosson

Characterization and Modeling of filled rubber submitted to thermal aging

R. Bouaziz[a], K.D. Ahose[a], S. Lejeunes[a,*], D. Eyheramendy[a], F. Sosson[b]

[a] *LMA, UMR 7031, Aix-Marseille Univ, CNRS, Centrale Marseille, Marseille, France*
[b] *SMAC, ZI Toulon Est, Toulon, France*

Abstract

This paper focuses on the characterization and the modeling of the behavior of butadiene rubber filled with carbon black that can be subjected to thermal aging phenomena. We consider only anaerobic thermal aging (i.e. we neglect diffusion effects) and we follow both the evolution of the behavior and that of the cross-linked network during aging with the help of mechanical and swelling tests. Based on experimental observations, we propose a fully coupled, finite strain, thermo-chemo-mechanical model that takes into account the chemo-physical evolution of the cross-linked network due to thermal aging. This model integrates a coupling between the chemo-physical evolution and the mechanical state that makes it possible to represent experimental observations. A specific strategy for the identification of material parameters is presented and provides promising results. Finite element implementation of the constitutive model is briefly described and allows to identify the chemo-mechanical coupling term from a creep test under thermal aging.

Key words: thermal aging, filled rubber, viscoelasticity, Payne effect, finite element

1. Introduction

For a large number of industrial applications, it is mandatory to estimate the lifetime of a part submitted to cyclic loading. Technical parts can undergo a large number of cycles under variable loading. Furthermore, due to environmental conditions or due to the severe loading conditions, these parts can be submitted to chemo-physical evolutions similar to those occurring during thermal aging. The sensitivity of the material to these phenomena requires to take into account these chemo-physical evolutions and their consequences within the modeling of the thermomechanical behavior to improve lifetime prediction of technical rubber products.

The carbon black filled butadiene rubber considered in this study is largely employed in these technical applications. This material exhibits a complex thermomechanical behavior during cyclic thermomechanical loading. Indeed, several phenomena are observed during dynamical loading tests that affect the thermo-mechanical properties of the material in question, e.g., Mullins effect, self-heating, amplitude dependency (Payne effect), etc. For a large number of cycles and under specific loading conditions, we also observe a phenomenon of stiffening that can be explained by the chemo-physical evolution of the material. This evolution is characterized by the increase in the concentration of the sulfur crosslinks and motivated by the self-heating phenomenon (see Lejeunes et al. (2018)). These phenomena can be interpreted as a coupling between the thermo-mechanical behavior of the rubber and thermal aging. In the literature, thermal aging of rubber has already been investigated in several studies and it is well known that the chemo-physical evolution of the network depends on several factors, such as the type of monomers and the intial curring system (e.g. Choi and Kim (2012); Pimolsiriphol et al. (2007)), the condition of aging (e.g. Mousa et al. (2002); Rabanizada et al. (2015); Tomer et al. (2007); Gac et al. (2012)) and on the mechanical state (e.g.

*Corresponding author
Email addresses: lejeunes@lma.cnrs-mrs.fr, tel: +33484525597 (S. Lejeunes)

Budrugeac (1995)). In order to gain better knowledge of these phenomena, we realized several thermo-chemo-mechanical tests on de-Mullinized tensile samples (samples submitted to pre-load/unload cycles to remove the Mullins effect) under different thermal-aging conditions (aging time, aging temperature). Among these tests, swelling tests were performed on several samples with different aging times to highlight the chemo-physical evolution during thermal aging. Static and dynamic loading tests were carried out at different temperatures, frequencies and static and dynamic amplitudes to study the impact of this chemo-physical evolution on the thermo-mechanical behavior of the material.

Regarding modeling, it has recently become of great interest to take into account these chemo-physical evolution phenomena within contiunuum mechanics. One or more local internal variables are introduced to describe the local evolution of the rubber network in a phenomenological sense. These local internal variables can be coupled directly or indirectly to the local thermo-mechanical state. In Gigliotti and Grandidier (2010), Gigliotti et al. (2011), Johlitz and Lion (2013), Johlitz et al. (2014), Lion and Johlitz (2012), the authors investigate thermo-oxidative phenomena occuring during aging of a polymer matrix, including chemical reactions with diffusion and mechanical coupling. Using internal variables allows to describe either the creation of new cross-link jonctions or the opposite phenomena of destruction of crosslinks or chain-scission that can occur during aging (e.g. Kari (2017),Musil et al. (2018)). All these authors show a collective willingness to take into account a strong coupling between chemical evolution and thermo-mechanical state in consistent thermodynamic formulations.

In N'Guyen et al. (2016), Lejeunes et al. (2018), a general modeling framework was proposed in order to describe thermo-chemo-mechanical couplings for nearly-incompressible materials at finite strain considering a nonlinear viscoelastic behavior. In this formulation, an appropriate chemical free energy is proposed that introduces an induction temperature below which no chemical reactions occur. Only one supplementary internal variable that describes the creation of new crosslinks is used and diffusion processes are neglected. The reciprocal coupling of the evolution of the chemical variable with the mechanical state is naturally introduced by considering the dependence of mechanical parameters on this internal variable and by introducing an original form of the chemical evolution law. The mechanical behavior is represented by a simple Zener rheological model. In the present study, we propose to adopt a similar approach and to combine it with the consitutive thermo-mechanical modeling that was proposed in Delattre et al. (2014), Delattre et al. (2016) for the same material. In the aforementioned papers, we introduced a phenomenological modeling of the Payne effect with the help of damage-like mechanisms combined with a generalized Maxwell representation of the viscosity. An original thermo-chemo-mechanical coupling law, considering a non Arrhenius behavior for the temperature dependency, is proposed. This law involves some chemical and coupled parameters that are identified from both swelling and mechanical results. The dependency of the different mechanical properties on both the chemical evolution and the temperature is also studied. The identified material parameters are tested to describe the experimental data that are used in the identification process and to predict other experimental results. A fully coupled finite elements implementation is briefly described. It allows us to completely identify all the material parameters, especially the parameter that couples the chemo-physical evolution and the mechanical state.

2. Material and methods

The material used in this study was butadiene rubber filled with nearly $40phr$ of carbon black. The precise chemical composition and the processing conditions are not given, due to industrial confidentiality reasons. This material was processed with efficient vulcanization system at 130°C. The processing time was determined to reach 98% of vulcanization determined by a rheometer. Prior to this experimental investigation of aging, we performed an experimental characterization of the dynamical behavior at different temperatures on the same material that can be found in Delattre et al. (2014, 2016). In this work, experimental tests were conducted on this material, already submitted to thermal aging tests at different temperatures, by means of electro-mechanic or hydraulic testing machines for monotonous and harmonic tensile tests at different aging times. These tests would allow us to study the impact of the thermal aging on the mechanical properties of the material. After each mechanical test, swelling tests were performed

(a) H2 specimen

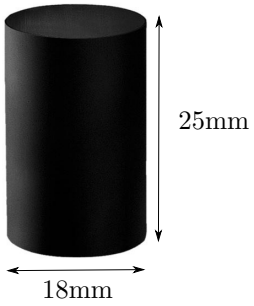

(b) Cylindrical specimen

Figure 1: Specimens used for mechanical characterization

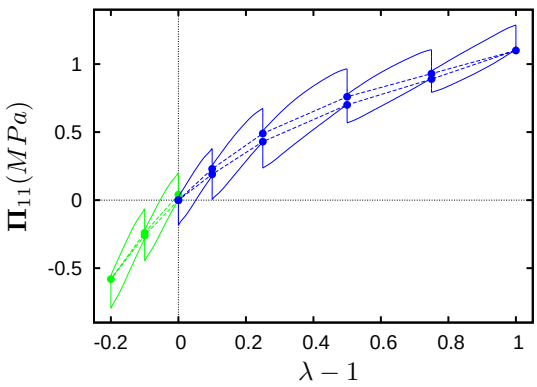

(a) Lading and unloading with multi-step tensile-relaxation tests

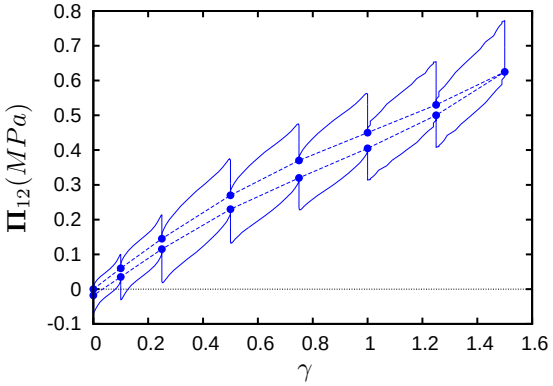

(b) Lading and unloading with multi-step shear-relaxation tests

Figure 2: Multi-step relaxation tests on virgin specimens at room temperature for two modes of loading: tension and shear (shear specimen are described in Delattre et al. (2016) and has not been used for aging due to metalic interfaces)

to analyze the evolution of the cross-linked network with the aging time. Combining mechanical tests and swelling tests allowed us to highlight the dependency of the mechanical properties upon the aging process.

2.1. Thermal aging tests

The thermal aging tests were carried out at three temperatures: 50°C, 70°C and 90°C. The aging test lasted 29 days at 70°C, 23 days at 90°C, and 31 days at 50°C. The specimens were placed in hermetic bags in which a vacuum was created using a pump in order to minimize the effects of oxidation. Our objective is to obtain homogenous ageing for stress-free ageing conditions such as to be able to relate the evolution of the mechanical behavior of the specimens to a thermal ageing state from standard mechanical tests. In the case of oxydative ageing strong gradients can be obtained and other characterization strategies can be used using local informations such as micro or nano indentation tests, e.g. Gigliotti et al. (2016); Minervino et al. (2014). Specimens were subjected to thermal aging tests followed by mechanical and chemical characterization tests. Each specimen was submitted to mass and dimension measurements before and after aging and no variation of mass or volume was observed. Each specimen was used once for mechanical and chemical tests and was not returned to the oven.

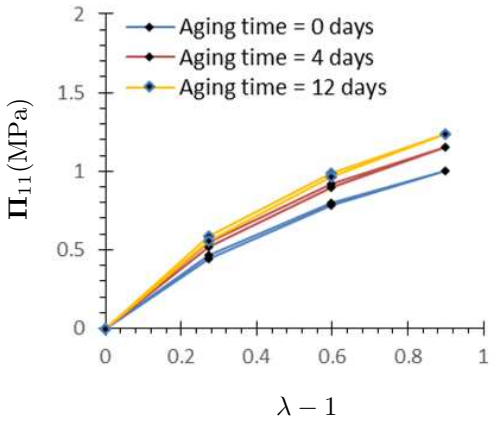

(a) Equilibrium hysteresis for samples aged at 70°C

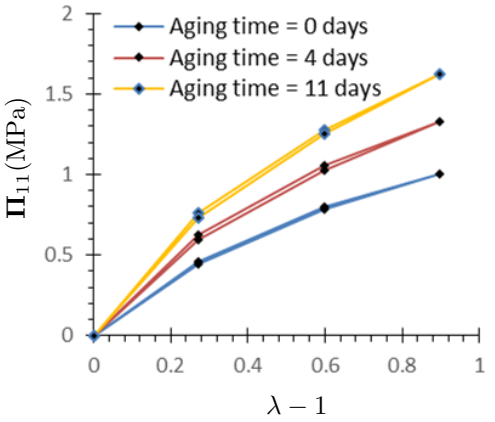

(b) Equilibrium hysteresis for samples aged at 90°C

Figure 3: Equilibrium hysterisis obtained at the ambient temperature after thermal aging

2.2. Mechanical behavior testing

The mechanical behavior of our material was characterized through static and dynamic tests, for each aging time, performed on cylindrical and tensile specimens (see figure 1). For tensile specimens (figure 1(a)), the static tests allow to study the equilibrium response and the evolution of static mechanical properties with the aging time. The equilibrium response was obtained from multi-step relaxation tests following the work of Lion (1996). Each relaxation test took 1 hour. It was possible to obtain the equilibrium hysteresis by joining the endpoints of relaxation tests (figure 2). Dynamic tests were designed to study the dissipative response and to determine the impact of the aging time on the dynamical properties. These tests were performed with different frequencies and static/dynamic amplitudes in order to study some phenomena that can occur during dynamic loading such as frequency dependency and Payne effect (amplitude dependency). The testing procedure was realized so as to minimize self-heating and thermal softening in order to focus on the quasi-isothermal material behavior. Each test was repeated twice on two different samples in order to obtain an averaged behavior. All tensile samples were subjected to several initial cycles with an amplitude that was higher than the maximum amplitude used for both static and dynamical characterization in order to eliminate the Mullins effect. The cylindrical specimens (figure 1(b)) were used in compressibility tests for studying the impact of thermal aging on the bulk modulus.

2.3. Swelling tests

To follow the evolution of the cross-linked network under the effect of aging, swelling tests were performed on small discs extracted from the previous aged specimens in order to ensure that thermal aging can be considered as homogeneous. The xylene has been used as a solvent during the swelling tests. The mass of each disk was recorded before and after swelling. The mass swelling ratio of each tensile specimen was computed from an average of at least 5 discs extracted from the specimen. Swelling ratio was found to be nearly homogeneous in the section of the tensile specimen that was no submitted to mechanical loading during aging. The swelling time was calibrated from a preliminary study on non aged samples.

3. Experimental characterization

3.1. Multi-step relaxation tests

From the multi-step relaxation tests, we can extract the equilibrium response (hysteresis) by interpolating the termination points of relaxation tests, as previously shown in figure 2. As it is shown in figure 3, the stiffness of the material increases with the thermal aging time. This result emphasizes that the process

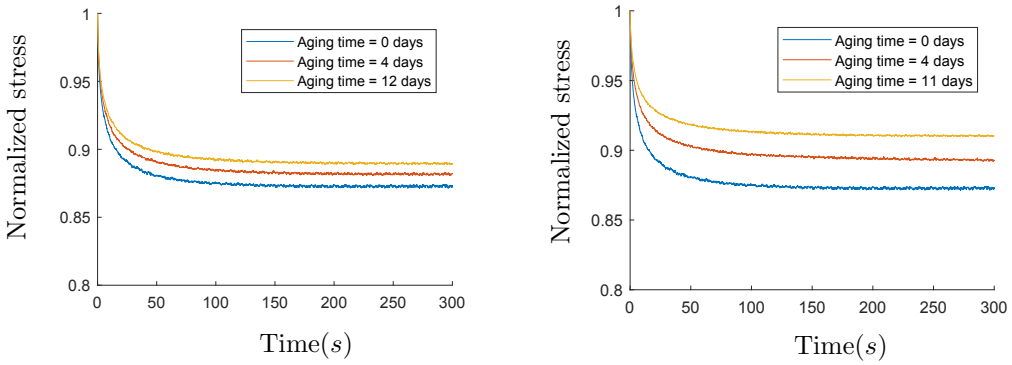

(a) Relaxation curves for samples aged at 70°C (b) Relaxation curves for samples aged at 90°C

Figure 4: Relaxation curves at 10mm displacement ($\lambda = 1.272$) for different aging times

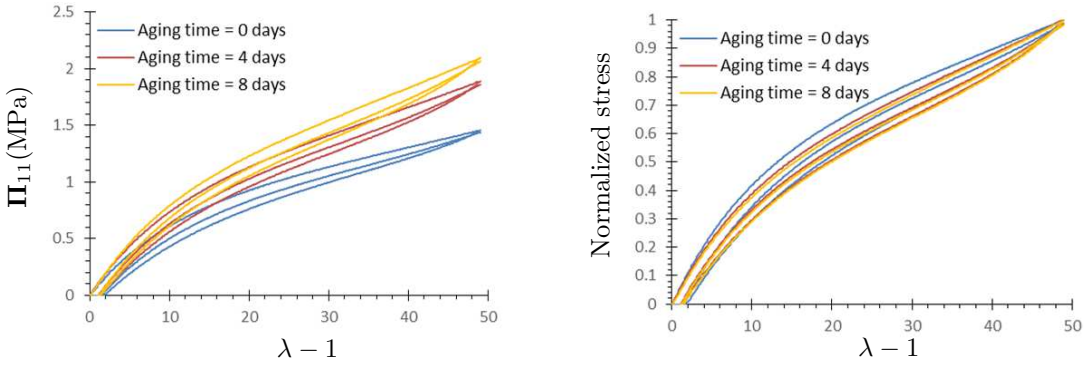

(a) Stiffness evolution (b) Normalized stress evolution

Figure 5: Mullins effect evolution with the aging time (Aging temperature = 90°C)

of chemical reorganization of crosslinks or network reformation during thermal aging is certainly the most important among other possible processes (network degradation, physical aging, etc.).

From the full relaxation results, we can also study the impact of thermal aging on the viscoelastic properties. Figure 4 shows different normalized relaxation curves for different aging times. We observe that the normalized relaxed stress decreases with the aging time. However, the relaxation time seems to be slightly increased with the aging time.

3.2. Mullins effect

Figure 5 shows the evolution of the Mullins effect with the aging time. Figure 5(a) shows the evolution of the first Piola Kirchhoff stress ($\mathbf{\Pi}_{11}$) as a function of deformation along the loading direction ($\lambda - 1$). As observed from multi-step relaxation tests, we can notice that the material stiffens with age and the Mullins effect seems to be the same for the three different aging times. In order to quantify the impact of aging on the Mullins effect, we have drawn the evolution of the normalized stress as a function of deformation (figure 5(b)). This figure shows that aging seems not to affect the Mullins effect.

3.3. Compressibility (oedometric) tests

In order to study the impact of thermal aging on the compressibility of the material, compressibility tests were conducted on cylindrical specimens $25mm$ in height and $18mm$ in diameter (see figure 1(b) and 6(a)) already aged at 70°C for different aging times (4, 8 and 14 days). These specimens were put in a steel die and the compression was applied by means of a rigid stamp. A small initial gap (less than 1mm) between

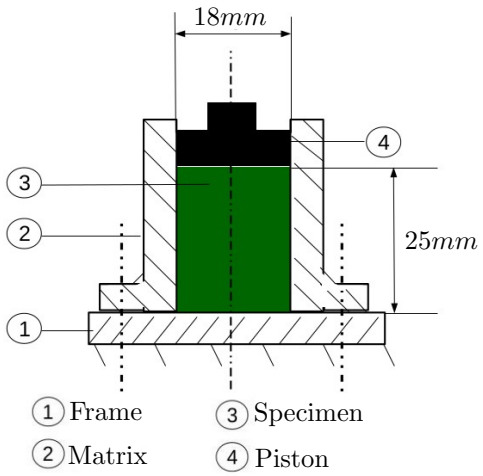

(a) Experimental setup of the compressibility test

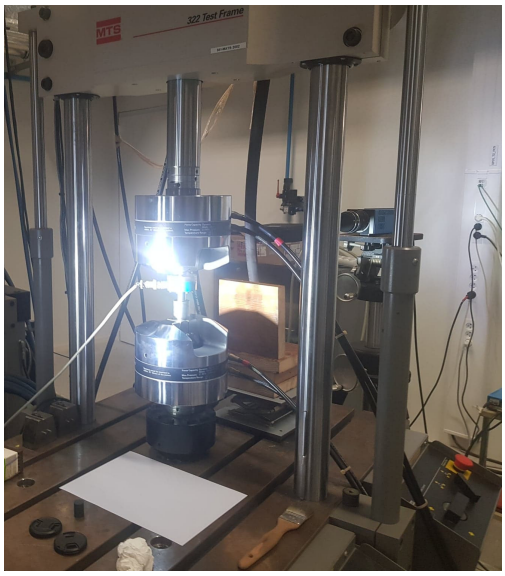

(b) MTS tensile machine equipped for compressibility testing

Figure 6: Experimental instrument for compressibility tests

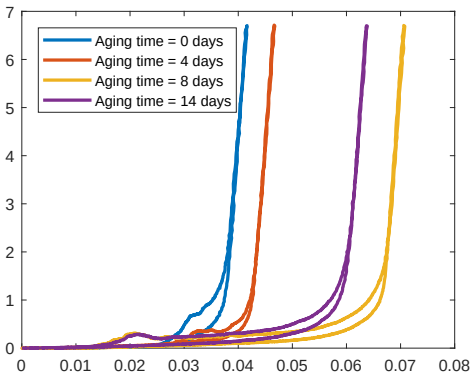

(a) Experimental results of compressibility tests

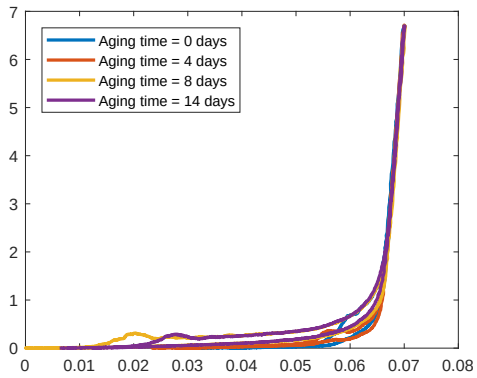

(b) Shifted experimental curves of compressibility

Figure 7: Compressibility loading and unloading responses at ambient temperature after thermal aging at 70°C

the specimen and the steel die allowed the specimens to be positioned inside the die. Figure 6(b) shows the machine used for these tests.

Figure 7(a) shows the evolution of the pressure as a function of volume variation for the non-aged specimen and the three aged specimens. In this study, we are only interested in the linear region of each curve, which corresponds to the hydrostatic regime. The bulk modulus is determined by evaluating the slope of the linear portion. By superimposing the linear portions of all the curves on one another, we notice that they coincide perfectly (see figure 7(b)). Consequently, we can conclude that the bulk modulus is not affected by thermal aging (at least for the first 14 days) and its value is estimated at 1.4 GPa.

3.4. Dynamic mechanical tests

To analyze the results of these tests, it is proposed to focus on the evolution of two characteristics obtained from stabilized cycles: the hysteresis area (in MPa), which is proportional to the dissipated energy

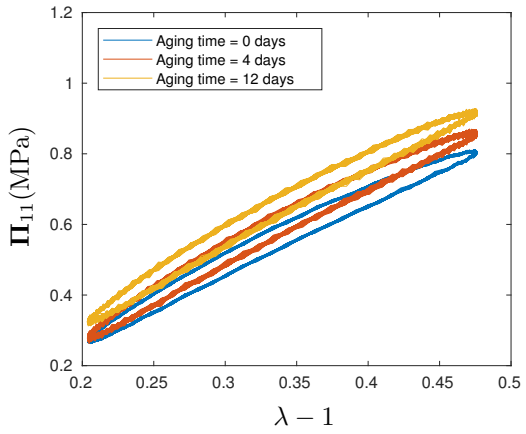

(a) Aging temperature = 70°C

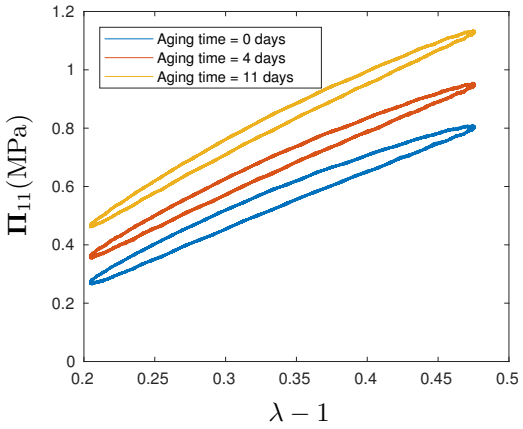

(b) Aging temperature = 90°C

Figure 8: Stabilized hysterisis at different aging times ($f = 10Hz$, Static amplitude = 0.34, Dynamic amplitude = 0.136)

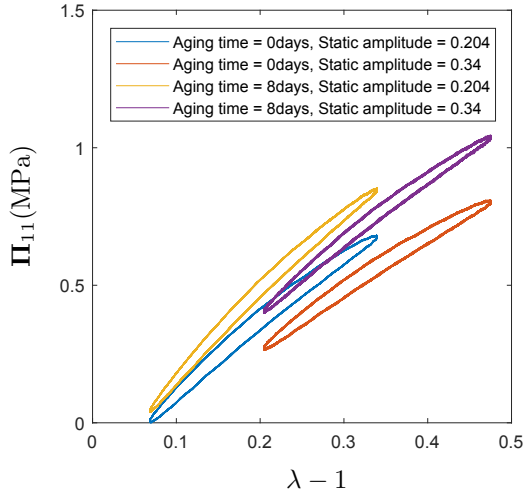

(a) Dynamic amplitude = 0.136, Aging time = 8 *days*

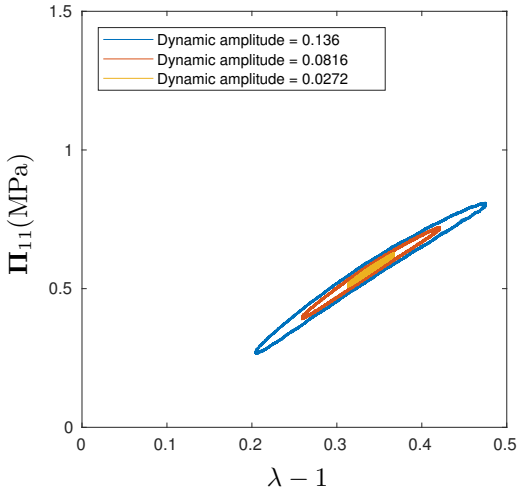

(b) Static amplitude = 0.34, Aging time = 0 *days*

Figure 9: Stabilized hysterisis at different static and dynamic amplitudes ($f = 10Hz$, Aging temperature = 90°C)

during a loading cycle, and a dynamic modulus (in MPa) which is defined as the slope of the secant to the hysteresis and which is characteristic of the dynamic stiffness of the material. Figure 8 depicts the evolution of equilibrium hysteresis as a function of the aging time for two different aging temperatures (70°C figure 8(a)) and 90°C (figure 8(b)) at the same frequency, static amplitude and dynamic amplitude. These figures show that the mean stress increases with aging time (translation of the equilibrium hysteresis to the top). It also shows an increase in the dynamic modulus with aging time (slight rotation of the equilibrium hysteresis in a counterclockwise direction), which can also be seen more clearly in figure 10(a). We can also notice that the hysteresis area decreases with aging time. These three observations are more conspicuous in figure 8(a) than in figure 8(b) because the material ages more quickly at 90°C than at 70°C.

Figure 9 shows the evolution of the stabilized hysteresis as a function of static and dynamic amplitudes for different aging times. In figure 9(a), we represent the stabilized hysteresis at two different static amplitudes and for two different aging times. In addition to the three observations depicted in figure 8, we also notice that the increase in the dynamic stiffness with aging time is greater for low static amplitudes than for

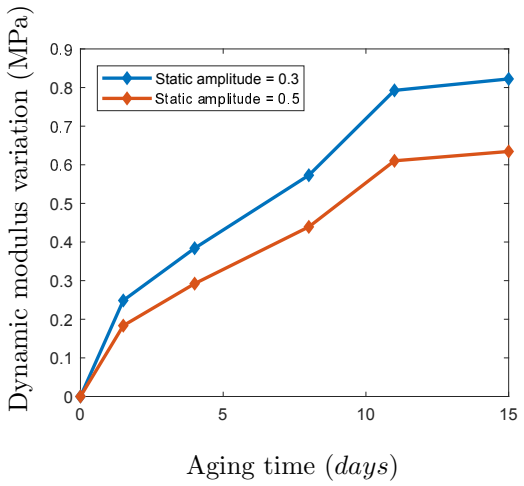

(a) Impact of the static amplitude on the dynamic modulus variation (dynamic amplitude = 0.136)

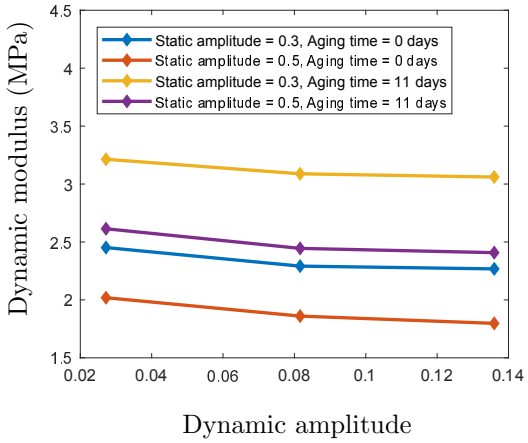

(b) Impact of the dynamic amplitude on the dynamic modulus at different static amplitudes and aging times

Figure 10: Impact of the static and dynamic amplitudes on dynamic modulus variation ($f = 3Hz$, Aging temperature = 90°C)

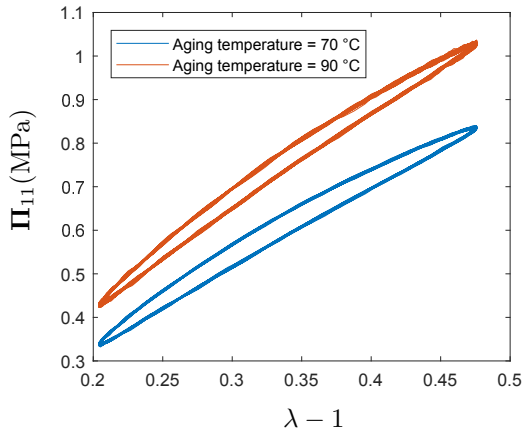

(a) $f = 3Hz$

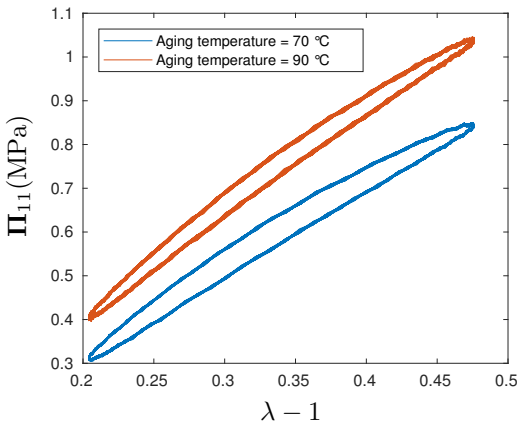

(b) $f = 10Hz$

Figure 11: Stabilized hysterisis at different aging temperatures (Aging time = 8 *days*, Static amplitude = 0.34, Dynamic amplitude = 0.136)

higher ones. In figure 9(b), we represent the stabilized hysteresis for three different dynamic amplitudes in the virgin state. Figure 10 depicts the evolution of the dynamic modulus according to the static and the dynamic amplitudes. In figure 10(a), we represent the evolution of the dynamic modulus variation, with respect to the virgin state, as a function of the aging time for two different static amplitudes. This shows that the evolution of the dynamic modulus is more substantial when the static amplitude is lower. Figure 10(b) shows that the dynamic softening effect (Payne effect) seems not to be very sensitive to aging (curves seem to be only vertically translated due to aging).

Figure 11 shows the impact of the aging temperature on the stabilized hysteresis for aged samples during the same aging time (height days for example) for the same static and dynamic amplitudes. The same observations depicted in figure 8 are noticed since that the speed of aging depends on the temperature.

Figure 12 depicts the evolution of the stabilized hysteresis as a function of frequency for the same static and dynamic amplitudes. It shows an increase in the dynamic modulus as a function of frequency. The

hysteresis area and the mean stress are still nearly the same. These results are observable in the two subfigures 11(a) and 11(b) which correspond to samples aged at 70°C for 12 days and samples aged at 90°C for 11 days, respectively.

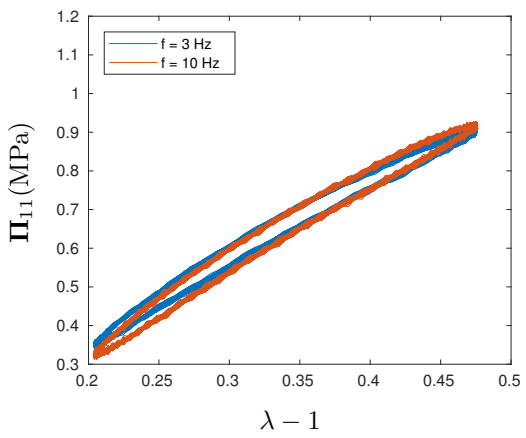

(a) Aging temperature = 70°C, Aging time = 12 *days*

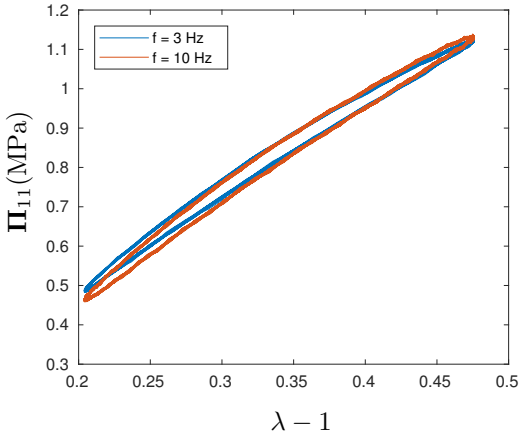

(b) Aging temperature = 90°C, Aging time = 11 *days*

Figure 12: Stabilized hysterisis at two different frequencies (Static amplitude = 0.34, Dynamic amplitude = 0.136)

3.5. Swelling tests

To characterize the chemical evolution as a function of aging time, we define the swelling ratio as follows:

$$R_s = (m_t - m_0)/(m_0) \tag{1}$$

where m_0 and m_t are the weight of the sample before and after swelling, respectively. The inverse of the swelling ratio is assumed to be proportional to the apparent cross-link density (Choi et al., 2010) according to Flory-Rehner theory (Flory and Rehner (1943)). Figure 13 shows the evolution of the inverse of the swelling ratio as a function of aging time at three different aging temperatures (50°C, 70°C and 90°C).

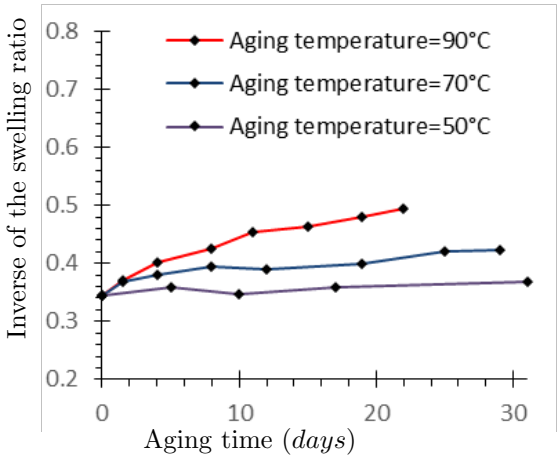

Figure 13: Evolution of the inverse of the swelling ratio as a function of aging time at two different aging temperatures

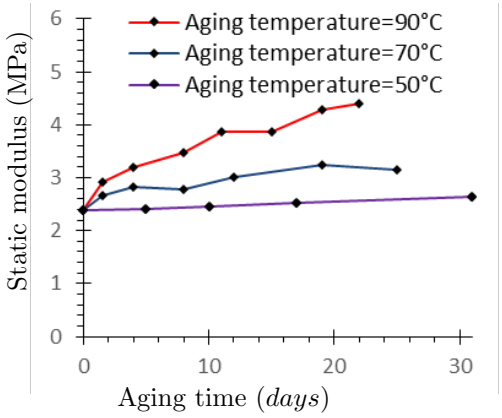

(a) Evolution of static modulus with aging time

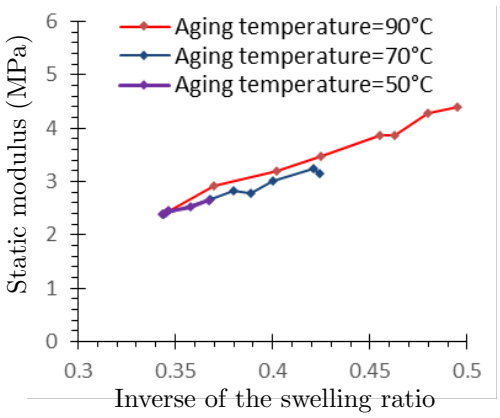

(b) Evolution of static modulus with the inverse of the swelling ratio

Figure 14: Static modulus evolution vs chemical evolution

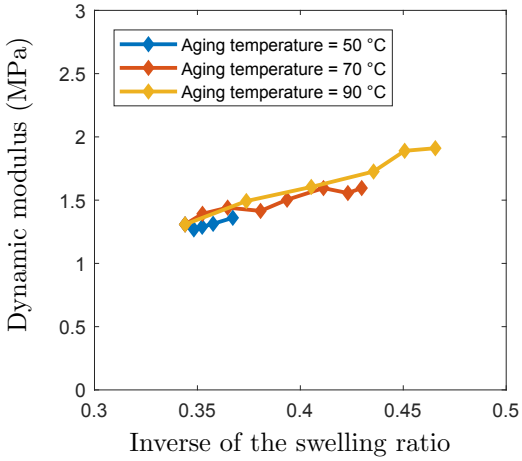

(a) Evolution of dynamic modulus with the inverse of the swelling ratio

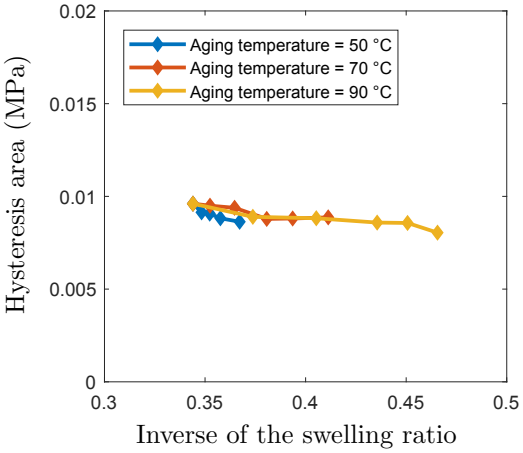

(b) Evolution of hysteresis area with the inverse of the swelling ratio

Figure 15: Dynamic properties evolution vs chemical evolution ($f = 0.1Hz$, Static amplitude = 0.517, Dynamic amplitude = 0.19)

From the previous mechanical results, we can easily establish the evolution of the mechanical properties with respect to the chemical evolution. Figure 14 shows the evolution of static modulus[1] as a function of aging time, figure 14(a), and as a function of the inverse of the swelling ratio, figure 14(b). The latter figure shows that the static stiffness is inversely proportional to the swelling ratio. As expected, this result is completely in accordance with the statistical theory of cross-linked network (e.g. Treloar (1943); Flory (1953)). In addition, this evolution is the same for the three temperatures of aging 50°C, 70°C and 90°C (the corresponding curves are superimposed on each other). The same result is observed for the dynamical modulus (see figure 15(a)). Therefore, the inverse of the swelling ratio seems to be a good candidate to describe the evolution of the cross-linked network at the macro scale.

[1]Static modulus is defined as the initial slope of the equilibrium hysteresis.

4. Constitutive Modeling

To take into account the thermal aging within a thermo-mechanical constitutive model, we propose to adopt the same approach used in N'Guyen et al. (2016); Lejeunes et al. (2018). A local chemo-physical evolution that describes aging kinetics is introduced by means of a chemical variable designated by $\xi(\mathbf{x}, t)$. The variable ξ is the local chemical conversion ($\xi \in [0, 1]$ and $\xi(\mathbf{x}, 0) = 0$) where $\mathbf{x}$ is the current position of a material point. This variable describes the increase in the apparent cross-link density during thermal aging. Other aging phenomena, such as destruction of cross-link or chain breakage or diffusion of species, are neglected here. However, as in Lejeunes et al. (2018); N'Guyen et al. (2016) the evolution of the apparent cross-link density depends on both thermal and mechanical states. For the thermo-mechanical part of the constitutive model, we adopt the same approach as proposed in Delattre et al. (2016), which considers multiple non-equilibrium responses represented by isochoric viscous over-stresses and introduces additional internal variables that take into account the dynamical softening due to the Payne effect.

4.1. Preliminary

We assume that ξ can be directly correlated to the local capacity of a material point to swell when put in a solvent. Therefore, we adopt the following definition for ξ:

$$\xi(\mathbf{x}, t) = \frac{Q(\mathbf{x}, t) - Q_0(\mathbf{x}, 0)}{Q_\infty(\mathbf{x}, \infty) - Q_0(\mathbf{x}, 0)} \tag{2}$$

where Q is the inverse of the swelling ratio ($Q = 1/R_s$), Q_0 is the inverse of the initial swelling ratio and Q_∞ is the maximum value of Q that the material can reach. This value is supposed to be reached at the infinity. Therefore, we can relate the experimental results of swelling directly to an internal variable. Using the Florry-Rehner theory of swelling (see Flory and Rehner (1943)) one can also relate the variable ξ and the apparent cross-link density (keeping in mind that the Flory-Rehner expression is based on an ideal, unfilled, amorphous network).

4.2. Kinematics

The proposed constitutive model is based on the thermodynamics of irreversible processes and on the local state assumption. The viscoelastic over-stresses are introduced through the help of intermediate configurations defined from the split of the deformation gradient $\mathbf{F}(\mathbf{X}, t)$, where $\mathbf{X}$ is the position of a material point in the reference configuration. To consider the nearly incompressible behavior, the deformation gradient $\mathbf{F}$ is split into a volumetric and an isochoric part. The isochoric part is also multiplicatively decomposed into purely isochoric elastic parts $\bar{\mathbf{F}}^i_{\mathbf{e}}(\mathbf{X}, t)$ and isochoric viscous parts $\bar{\mathbf{F}}^i_{\mathbf{v}}(\mathbf{X}, t)$ where i stands for the i^{th} decomposition:

$$\begin{cases} \mathbf{F} = \mathbf{F}^{vol}\bar{\mathbf{F}} \\ \mathbf{F}^{vol} = J^{1/3}\mathbf{1} \\ \bar{\mathbf{F}} = J^{-1/3}\mathbf{F} = \bar{\mathbf{F}}^i_{\mathbf{e}}\bar{\mathbf{F}}^i_{\mathbf{v}} \end{cases} \tag{3}$$

where:

- $\mathbf{F}^{vol}$ and $\bar{\mathbf{F}}$ are, respectively, the volumetric and the isochoric parts of the deformation gradient $\mathbf{F}$.
- $\mathbf{1}$ is the second order unit tensor.
- $J = \det(\mathbf{F})$ is the jacobian of $\mathbf{F}$ that corresponds to the total volume variation.

From physical measurements (mass and dimension) of specimens before and after aging we did not observe any variation of mass or volume due to aging. Therefore, we assume that the volume variation J can only

be attributed to thermal dilatation or mechanical compressibility. We adopt the following decomposition of the volume variation: $J = J_\Theta J_m$, with

$$J_\Theta = 1 + \alpha_\Theta(\Theta - \Theta_0) \tag{4}$$

$$J_m = \frac{J}{J_\Theta} \tag{5}$$

where α_Θ is the thermal expansion coefficient and Θ_0 is the reference temperature. The previous linear expansion relation is motivated by experimental evidence that we have obtained from dilatometry experiments.

4.3. Thermodynamics

In the following, we adopt the hybrid free energy concept as already presented in Lion et al. (2014); Lejeunes et al. (2018); Lejeunes and Eyheramendy (2018). The main idea is to formulate the free energy from standard state and internal variables. The volume dependency is replaced with a pressure like variable designated by q. This formalism can be viewed as a generalization of the partial Legendre transform of the free energy.

The hybrid free specific energy is assumed as follows:

$$\varphi(\bar{\mathbf{B}}, \bar{\mathbf{B}}^i_{\mathbf{e}}, \omega_i, q, \xi, \Theta) = \varphi_{iso}(\bar{\mathbf{B}}, \bar{\mathbf{B}}^i_{\mathbf{e}}, \omega_i, \xi, \Theta) + \varphi_{vol}(q, \Theta) + \varphi_{therm}(\Theta) + \varphi_{chem}(\xi, \Theta) \tag{6}$$

where $\bar{\mathbf{B}} = \bar{\mathbf{F}} \cdot \bar{\mathbf{F}}^{\mathrm{T}}$ and $\bar{\mathbf{B}}^i_{\mathbf{e}} = \bar{\mathbf{F}}^i_{\mathbf{e}} \cdot \bar{\mathbf{F}}^{i^{\mathrm{T}}}_{\mathbf{e}}$ are the isochoric left Cauchy Green tensor and the i^{th} elastic isochoric left Cauchy Green tensor, ω_i are scalar damage-like internal variables (to take into account the Payne effect, see Delattre et al. (2016)).

The additive splitting of eq. (6) is motivated by the fact that there can exist purely thermal variations that are stress-free for which no chemical reaction occurs (contribution of φ_{therm}). Themo-chemical evolutions that are stress-free can also be observed (contribution φ_{chem}) and finally thermo-mechanical states can also exist without any chemical reactions occurring. Furthermore, due to the huge difference in stiffness for hydrostatic or isochoric states we follow Flory (1961) and we adopt an isochoric/volumetric split for the remaining part of the hybrid energy (contributions of φ_{iso} and φ_{vol}). We do not observe impact of the aging on the thermal properties of the material (heat capacity and thermal dilatation), therefore φ_{therm} is assumed to depend only on Θ. It is the same for the volumetric contribution, therefore φ_{vol} depends only on the pressure-like variable q and the temperature.

The hybrid energy approach requires to define a supplementary potential, β, which allows to relate q, J and Θ with a constitutive law (or a supplementary flow rule if one considers dissipative mechanisms in volume, cf Lejeunes and Eyheramendy (2018) for more details). The hybrid energy φ can be related to the Helmholtz free energy ψ through the relation:

$$\psi(\bar{\mathbf{B}}, \bar{\mathbf{B}}^i_{\mathbf{e}}, \omega_i, J, \xi, \Theta) = \varphi(\bar{\mathbf{B}}, \bar{\mathbf{B}}^i_{\mathbf{e}}, \omega_i, q, \xi, \Theta) - \beta(J, \Theta, q) \tag{7}$$

The potential β is chosen as in Lejeunes and Eyheramendy (2018):

$$\beta = \frac{q(1 - J_m)}{\rho_0} \tag{8}$$

where ρ_0 is the initial mass density ($\rho_0 = J\rho$).

The combination of the first and the second law of thermodynamics leads to the following inequality (Clausius-Duhem form):

$$\begin{aligned}
\phi = &\left(\boldsymbol{\sigma} - 2\rho \left(\bar{\mathbf{B}} \frac{\partial \varphi}{\partial \bar{\mathbf{B}}} + \sum_{i=1}^{N} \bar{\mathbf{B}}^i_{\mathbf{e}} \frac{\partial \varphi}{\partial \bar{\mathbf{B}}^i_{\mathbf{e}}} \right)^{\mathrm{D}} + J\rho \frac{\partial \beta}{\partial J} \mathbf{1} \right) : \mathbf{D} - \rho \left(s + \frac{\partial \varphi}{\partial \Theta} - \frac{\partial \beta}{\partial \Theta} \right) \dot{\Theta} \\
&+ 2\rho \sum_{i=1}^{N} \left(\bar{\mathbf{B}}^i_{\mathbf{e}} \frac{\partial \varphi}{\partial \bar{\mathbf{B}}^i_{\mathbf{e}}} \right) : \bar{\mathbf{D}}^{\mathbf{o}\,i}_{\mathbf{v}} - \rho \left(\frac{\partial \varphi}{\partial q} - \frac{\partial \beta}{\partial q} \right) \dot{q} - \rho \sum_{i=1} \frac{\partial \varphi}{\partial \omega_i} \dot{\omega}_i - \rho \frac{\partial \varphi}{\partial \xi} \dot{\xi} - \frac{\mathrm{grad}_{\boldsymbol{x}} \Theta}{\Theta} \mathbf{q}_\Theta \geq 0 \\
&\forall \mathbf{D}, \dot{\Theta}, \bar{\mathbf{D}}^{\mathbf{o}\,i}_{\mathbf{v}}, \dot{q}, \mathbf{q}_\Theta, \dot{\omega}_i, \dot{\xi}
\end{aligned} \tag{9}$$

where ϕ is the total dissipation, $\boldsymbol{\sigma}$ is the Cauchy stress, $\mathbf{D}$ is the Eulerian strain rate: $\mathbf{D} = 1/2(\mathbf{L} + \mathbf{L}^{\mathrm{T}})$ with $\mathbf{L} = \dot{\mathbf{F}}\mathbf{F}^{-1}$, ρ is the current density, s is the specific entropy, $\mathbf{q}_\Theta$ is the Eulerian heat flux, $\bar{\mathbf{D}}^{\mathbf{o}^i}_{\mathbf{v}}$ is the i^{th} objective Eulerian strain rate, defined from:

$$\bar{\mathbf{D}}^{\mathbf{o}^i}_{\mathbf{v}} = \bar{\mathbf{R}}^i_{\mathbf{e}} \bar{\mathbf{D}}^i_{\mathbf{v}} \bar{\mathbf{R}}^{i^{\mathrm{T}}}_{\mathbf{e}} \tag{10}$$

where $\bar{\mathbf{R}}^i_{\mathbf{e}}$ comes from the polar decomposition $\bar{\mathbf{F}}^i_{\mathbf{e}} = \bar{\mathbf{V}}^i_{\mathbf{e}} \bar{\mathbf{R}}^i_{\mathbf{e}}$. Assuming that the dissipation is only due to thermal diffusion, mechanical viscosity including Payne effect and chemical evolution, the following constitutive equations can be obtained from eq. (9):

$$\boldsymbol{\sigma} = \overbrace{2\rho \left(\bar{\mathbf{B}} \frac{\partial \varphi_{iso}}{\partial \bar{\mathbf{B}}} \right)^{\mathrm{D}} + \frac{q}{J_\Theta} \mathbf{1}}^{\boldsymbol{\sigma}_{eq}} + \sum_{i=1}^{N} \overbrace{2\rho \left(\bar{\mathbf{B}}^i_{\mathbf{e}} \frac{\partial \varphi_{iso}}{\partial \bar{\mathbf{B}}^i_{\mathbf{e}}} \right)^{\mathrm{D}}}^{\boldsymbol{\sigma}^i_v} \tag{11}$$

$$s = -\frac{\partial \varphi_{iso}}{\partial \Theta} - \frac{\partial \varphi_{vol}}{\partial \Theta} - \frac{\partial \varphi_{chem}}{\partial \Theta} - \frac{\partial \varphi_{therm}}{\partial \Theta} + \frac{q}{\rho_0} \frac{J \alpha_\Theta}{J^2_\Theta} \tag{12}$$

$$\frac{\partial \varphi_{vol}}{\partial q} = \frac{\partial \beta}{\partial q} = \frac{(1 - J_m)}{\rho_0} \tag{13}$$

where $\boldsymbol{\sigma}_{eq}$ is the equilibrium stress obtained at time-infinity at which the total stress $\boldsymbol{\sigma}$ is totally relaxed: $\boldsymbol{\sigma}_{eq} = \boldsymbol{\sigma}(t \to \infty)$, $\boldsymbol{\sigma}^i_v$ is the i^{th} viscous (non-equilibrium) stress: $\boldsymbol{\sigma}^i_v(t \to \infty) = 0$. Equation (13) is a constitutive equation for q and we can see from eq. (11) that the hydrostatic pressure is defined from $p = q/J_\Theta$.

We consider that the internal variables evolve independently from each other (e.g. Germain et al. (1983)). Then, the positiveness of each dissipation term is independently required. From eq. (9), we obtain the following inequalities:

$$\phi^i_{vis} = 2\rho \left(\bar{\mathbf{B}}^i_{\mathbf{e}} \frac{\partial \varphi_{iso}}{\partial \bar{\mathbf{B}}^i_{\mathbf{e}}} \right) : \bar{\mathbf{D}}^{\mathbf{o}^i}_{\mathbf{v}} = \boldsymbol{\sigma}^i_v : \bar{\mathbf{D}}^{\mathbf{o}^i}_{\mathbf{v}} \geq 0 \qquad \forall \bar{\mathbf{D}}^{\mathbf{o}^i}_{\mathbf{v}} \qquad i = 1..N \tag{14}$$

$$\phi^i_{payne} = -\rho \frac{\partial \varphi_{iso}}{\partial \omega^i} \dot{\omega}^i = A_\omega \dot{\omega}^i \geq 0 \qquad \forall \dot{\omega}^i \qquad i = 1..N \tag{15}$$

$$\phi_\xi = -\rho \frac{\partial \varphi}{\partial \xi} \dot{\xi} = A_\xi \dot{\xi} \geq 0 \qquad \forall \dot{\xi} \tag{16}$$

$$\phi_\Theta = \left(-\frac{\mathrm{grad}_{\boldsymbol{x}} \Theta}{\Theta} \right) \mathbf{q}_\Theta = A_\Theta \mathbf{q}_\Theta \geq 0 \qquad \forall \mathbf{q}_\Theta \tag{17}$$

$$\phi = \sum_{i=1}^{N} \phi^i_{vis} + \sum_{i=1}^{N} \phi^i_{payne} + \phi_\xi + \phi_\Theta \geq 0 \tag{18}$$

where $\boldsymbol{\sigma}^i_v, A_\omega, A_\xi, \mathbf{A}_\Theta$ are thermodynamic forces associated with the thermodynamic fluxes $\bar{\mathbf{D}}^{\mathbf{o}^i}_{\mathbf{v}}, \dot{\omega}^i, \dot{\xi}, \mathbf{q}_\Theta$. For the thermal dissipation term, eq. 17, we assume an isotropic Fourier conduction law such that:

$$\mathbf{q}_\Theta = -k_\Theta \mathrm{grad}_{\boldsymbol{x}} \Theta \tag{19}$$

the conductivity coefficient k_Θ is assumed to be constant and not affected by aging (this assumption is not supported by experimental evidence because we did not do such experiments).

The first thermodynamics principle (energy conservation) can be written as follows in the current configuration:

$$\rho \Theta \dot{s} = \sum_{i=1}^{N} \phi^i_{vis} + \sum_{i=1}^{N} \phi^i_{payne} + \phi_\xi + \rho r - \mathrm{div}_{\mathbf{x}} \mathbf{q}_\Theta \tag{20}$$

where $\mathrm{div}_{\mathbf{x}}$ is the Eulerian divergence, r is an external heat supply term defined by unit of mass. Computing the material time derivative of entropy from its constitutive equation, eq. (12), we can obtain the following local form of the heat balance:

$$\rho C_p \dot{\Theta} = \sum_{i=1}^{N} \phi_{vis}^i + \sum_{i=1}^{N} \phi_{payne}^i + \phi_\xi + \rho r + l_m + l_q + l_\xi - \mathrm{div}_{\mathbf{x}} \mathbf{q}_\Theta \tag{21}$$

where C_p is the isobaric heat capacity:

$$C_p = -\Theta \left(\frac{\partial^2 \varphi}{\partial \Theta^2} - \frac{\partial^2 \beta}{\partial \Theta^2} \right) = -\Theta \left(\frac{\partial^2 \varphi}{\partial \Theta^2} + \frac{2Jq\alpha_\Theta^2}{J_\Theta^3 \rho_0} \right) \tag{22}$$

the coupling terms l_m, l_q and l_ξ are defined from:

$$\begin{aligned} l_m &= \Theta \frac{\partial \boldsymbol{\sigma}}{\partial \Theta} : \mathbf{D} - \Theta \sum_{i=1}^{N} \frac{\partial \boldsymbol{\sigma}_v^i}{\partial \Theta} : \bar{\mathbf{D}}_{\mathbf{v}}^{\mathbf{o}^i} + \Theta \sum_{i=1}^{N} \frac{\partial A_\omega}{\partial \Theta} \dot{\omega}_i \\ l_q &= -\Theta \frac{\alpha_\Theta}{J_\Theta^2} \dot{q} \\ l_\xi &= \frac{\partial A_\xi}{\partial \Theta} \dot{\xi} \end{aligned} \tag{23}$$

4.4. Proposition of a thermo-chemo-viscoelastic model

We consider the case of isotropic behavior and we propose to adopt the following potentials:

$$\rho_0 \varphi_{iso} = C_{10}(\xi, \Theta) \left(I_1(\bar{\mathbf{B}}) - 3 \right) + C_{01}(\xi, \Theta) \left(I_2(\bar{\mathbf{B}}) - 3 \right) + \sum_{i=1}^{N} \omega_i \frac{\mu_i(\xi, \Theta)}{2} (I_1(\bar{\mathbf{B}}_{\mathbf{e}}^i) - 3) \tag{24}$$

$$\rho_0 \varphi_{therm} = C_0 \left(\Theta - \Theta_0 - \Theta \log \left(\frac{\Theta}{\Theta_0} \right) \right) - C_1 \frac{(\Theta - \Theta_0)^2}{2\Theta_0} \tag{25}$$

$$\rho_0 \varphi_{chem} = C_2 \left(\tanh \left(m \frac{\Theta - \Theta_{ind}}{\Theta_{ind}} \right) \frac{(1-\xi)^{n+1}}{n+1} - \tanh \left(m \frac{\Theta_0 - \Theta_{ind}}{\Theta_{ind}} \right) \right) \tag{26}$$

$$\rho_0 \varphi_{vol} = -k \left(\exp \left(\frac{q}{k} \right) \right) + q + k \tag{27}$$

where C_{10}, C_{20} are the Mooney-Rivlin coefficients that are assumed to be dependent on ξ and Θ, μ_i is the i^{th} shear modulus that depends on ξ and Θ. The bulk modulus, k, is assumed to be independent of these variables. I_1 and I_2 are respectively the first and the second invariant of a strain tensor. C_0 and C_1 define the isobaric heat capacity (which is assumed to be only temperature dependent in this paper), C_2 is a heat-like coefficient related to the chemical process, Θ_{ind} is an induction temperature for the chemical process[2], n is a chemical parameter and m a dimensionless parameter.

4.4.1. Equilibrium contribution

Using the previous definition, from eq. (11), the equilibrium stress is written as:

$$\boxed{\boldsymbol{\sigma}_{eq} = 2J^{-1} C_{10}(\xi, \Theta) \bar{\mathbf{B}}^{\mathrm{D}} + 2J^{-1} C_{01}(\xi, \Theta) (I_1(\bar{\mathbf{B}}) \bar{\mathbf{B}} - \bar{\mathbf{B}}^2)^{\mathrm{D}} + \frac{q}{J_\Theta} \mathbf{1}} \tag{28}$$

and using eqs. (13) and (27), we obtain the following compressibility law:

$$\boxed{J_m = \exp \left(\frac{q}{k} \right)} \tag{29}$$

[2]No chemical reactions are assumed to occur if $\Theta < \Theta_{ind}$

4.4.2. Visco-elastic contribution

From eq. (11), we can calculate the i^{th} viscous stress, which is defined by:

$$\boxed{\boldsymbol{\sigma}_v^i = J^{-1}\mu_i(\xi,\Theta)\omega_i \bar{\mathbf{B}}_{\mathbf{e}}^{i\ \mathrm{D}}} \qquad i = 1..N, \quad \omega_i \in [0,1] \tag{30}$$

We consider a Maxwell-like flow rule for viscosity as follows:

$$\bar{\mathbf{D}}_{\mathbf{v}}^{\mathbf{o}^i} = \frac{1}{\eta_i(\xi,\Theta,\omega_i)}\boldsymbol{\sigma}_v^i \quad i = 1..N \tag{31}$$

where $\eta_i(\xi,\Theta,\omega_i)$ is the i^{th} viscosity parameter. The positiveness of the viscous dissipation terms, ϕ_{vis}^i, can be easily shown by introducing (31) in (14). The Maxwell flow rule can also be reformulated using the following relation (that comes from the time differentiation of $\bar{\mathbf{B}}_{\mathbf{e}}^i$ and the multiplicative split of the deformation gradient):

$$\dot{\bar{\mathbf{B}}}_{\mathbf{e}}^{\ i} = \mathbf{L}\bar{\mathbf{B}}_{\mathbf{e}}^i + \bar{\mathbf{B}}_{\mathbf{e}}^i\mathbf{L}^{\mathrm{T}} - 2\bar{\mathbf{V}}_{\mathbf{e}}^i\bar{\mathbf{D}}_{\mathbf{v}}^{\mathbf{o}^i}\bar{\mathbf{V}}_{\mathbf{e}}^i \tag{32}$$

combining eqs. (32) and (31), we obtain:

$$\boxed{\begin{array}{l}\dot{\bar{\mathbf{B}}}_{\mathbf{e}}^{\ i} = \mathbf{L}\bar{\mathbf{B}}_{\mathbf{e}}^i + \bar{\mathbf{B}}_{\mathbf{e}}^i\mathbf{L}^{\mathrm{T}} - \dfrac{2}{3}(\mathbf{1}:\mathbf{L})\bar{\mathbf{B}}_{\mathbf{e}}^i - \dfrac{1}{J\tau_i}\bar{\mathbf{B}}_{\mathbf{e}}^i\bar{\mathbf{B}}_{\mathbf{e}}^{i\ \mathrm{D}} \\ \bar{\mathbf{B}}_{\mathbf{e}}^i(t=0) = \mathbf{1}\end{array}} \quad i = 1..N \tag{33}$$

where $\tau_i = \eta_i/2\omega_i\mu_i$ is a characteristic time of the viscoelasticity phenomena, linked to the i^{th} viscous stress.

4.4.3. Modeling of the Payne effect

The Payne effect is a phenomenon particular to rubber (especially filled rubber) that occurs during cyclic loading and characterized by a dynamical softening. This behavior is attributed to the evolution of the microstructure of the material, such as breakage/reformation of weak physical bonds. This approach was formulated by Kraus and co-workers (Kraus et al. (1966)) and enriched later by many authors (see for instance Ulmer (1996)).

The Payne effect impacts the viscoelastic storage modulus by increasing or decreasing the loading amplitude, which can be viewed as local damage/reforming mechanism. This effect occurs only above a specific amplitude. At a fixed higher amplitude, the material stabilizes after a few cycles. In the proposed model, only the damage mechanism is considered (increasing amplitudes). The variables ω_i are decreasing variables which take one as initial value. Using the definition of eq. (24) in (15), we obtain the following inequality:

$$\phi_{payne}^i = -J^{-1}\frac{\mu_i(\xi,\Theta)}{2}(I_1(\bar{\mathbf{B}}_{\mathbf{e}}^i) - 3)\dot{\omega}_i \geq 0 \qquad i = 1..N \quad \forall\dot{\omega}_i \tag{34}$$

which is equivalent to $\dot{\omega}_i \leq 0$.

Assuming that this effect does not depend on the applied strain rate or on the temperature, the following evolution law is proposed, which fulfills the previous thermodynamic requirement:

$$\boxed{\dot{\omega}_i = -\frac{1}{h_i}\left\langle \omega_i - \left(\frac{3}{I_1(\bar{\mathbf{B}})}\right)^{r_i}\right\rangle, \quad \omega_i(t=0) = 1} \quad i = 1..N \tag{35}$$

4.4.4. Chemical evolution due to aging

The thermodynamic force associated with the chemical aging, A_ξ, can be obtained from:

$$\begin{aligned} A_\xi = -\rho\frac{\partial\varphi}{\partial\xi} =& J^{-1}C_2\tanh\left(m\frac{\Theta-\Theta_{ind}}{\Theta_{ind}}\right)(1-\xi)^n - J^{-1}\frac{\partial C_{10}}{\partial\xi}(I_1(\bar{\mathbf{B}})-3) \\ &- J^{-1}\frac{\partial C_{01}}{\partial\xi}(I_2(\bar{\mathbf{B}})-3) - J^{-1}\sum_{i=1}^{N}\omega_i\frac{1}{2}\frac{\partial\mu_i}{\partial\xi}(I_1(\bar{\mathbf{B}}_{\mathbf{e}}^i)-3) \end{aligned} \tag{36}$$

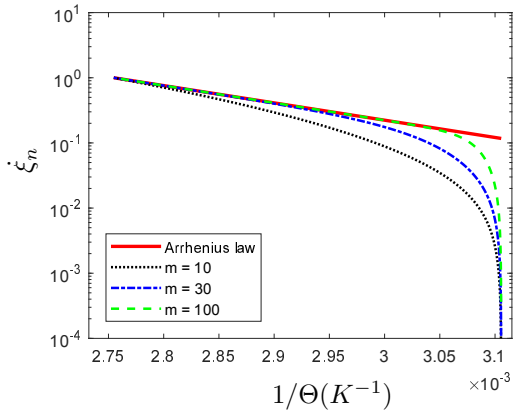

Figure 16: Comparison between the Arrhenius law and the proposed model

As in N'Guyen et al. (2016) and in order to fulfill the positiveness requirement of the chemical dissipation defined by (16), we propose the following chemical evolution equation:

$$\boxed{\dot{\xi} = k_\xi(\Theta)\,\langle A_\xi \rangle} \tag{37}$$

The term $k_\xi(\Theta)$ is defined from Arrhenius behavior:

$$k_\xi(\Theta) = A \exp^{-\frac{E_a}{R\Theta}} \tag{38}$$

where $R = 8.314 J/mol/K$ is the ideal gas constant, E_a is an activation energy and A is a kinetic parameter[3].

It can be noticed from eqs. (36) and (37) that if C_{10}, C_{01} and μ_i are increasing functions of ξ (stiffening behavior during aging), the chemical aging evolution will be lower under aging conditions with a non null mechanical load compared to a stress-free configuration (depending on the order of magnitude of each term in eq. (37)). It can also be noticed that for stress-free conditions, the chemical evolution law reduces to:

$$\dot{\xi} = J_\Theta^{-1} A\, C_2 \exp^{-\frac{E_a}{R\Theta}} \left\langle \tanh\left(m \frac{\Theta - \Theta_{ind}}{\Theta_{ind}} \right) \right\rangle (1-\xi)^n \tag{39}$$

It can be noticed that eq. (39) defines a non Arrhenius behavior when Θ is lower than or close to the induction temperature and tends to Arrhenius behavior when Θ is higher than the induction temperature. The parameter m makes it possible to play with the non-linearity, as can be seen in figure 16.

Compared with Arrhenius law, the proposed model allows to take into account the thermodynamics state with and without chemical reactions in a consistent manner by introducing this non Arrhenius behavior that depends on an induction temperature.

5. Material parameter identification

The chemical, hyperelastic and viscoelastic parameters are identified separately by solving constrained minimization problems defined by:

$$\min_{p \in \Omega} \left[Err(p) \right] \tag{40}$$

where $Err(p)$ is the mean square error between the experimental data and the corresponding semi-analytical representation, p is a parameter vector and Ω defines the constraints for each parameter. These problems are solved with the help of $Matlab\,2017b$ ©.

[3]Parameters A and C_2 allow us to play with the relative influence of mechanical terms in the chemical evolution law and also control the chemical heat coupling terms in the heat equation.

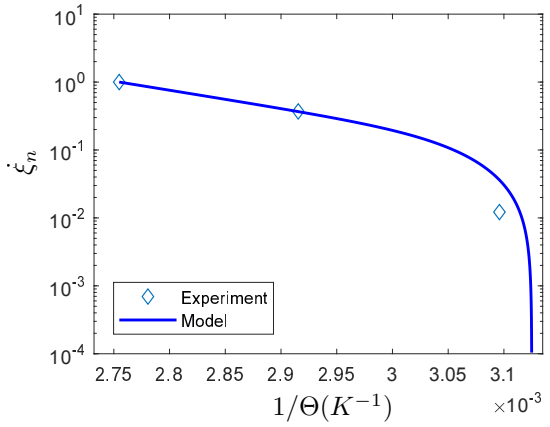

(a) Identification of the kinetic part, parameters E_a, m

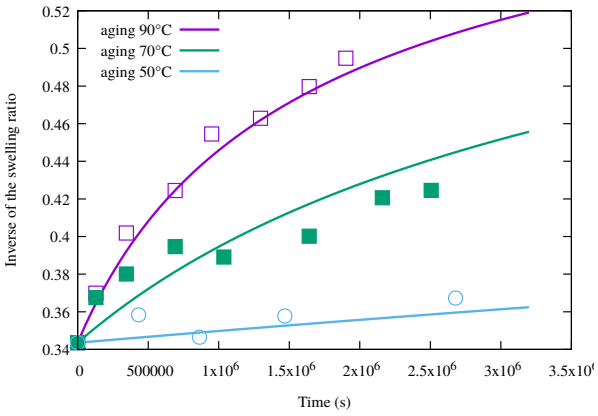

(b) Identification of all other chemical parameters AC_2, n, Q_∞

Figure 17: Comparison between the proposed model and the experimental data

5.1. Identification of chemical parameters

The chemical parameters are identified from the experimental results of swelling tests for the three aging temperatures (50°, 70° and 90°). Considering that the reaction order is higher than 1 ($n > 1$), the integration of eq (39) leads to the following expression (stress-free case):

$$\xi(t) = 1 - \left(1 + J_\Theta^{-1} A\, C_2 \exp^{-\frac{E_a}{R\Theta}} \left\langle \tanh\left(m \frac{\Theta - \Theta_{ind}}{\Theta_{ind}}\right)\right\rangle (n-1)t\right)^{\frac{1}{1-n}} \tag{41}$$

From equations (2) and (41), we obtain the following relationship:

$$Q(t) = (Q_\infty - Q_0)\left(1 - \left(1 + J_\Theta^{-1} A\, C_2 \exp^{-\frac{E_a}{R\Theta}} \left\langle \tanh\left(m \frac{\Theta - \Theta_{ind}}{\Theta_{ind}}\right)\right\rangle (n-1)t\right)^{\frac{1}{1-n}}\right) + Q_0 \tag{42}$$

Q_∞ is a constant and does not depend on the aging temperature. n is also supposed to be the same for the three aging temperatures.

1. **Determination of E_a and m**

   In order to determine the activation energy E_a and the parameter m, we start by approximating the experimental data of Q_Θ with a regular function (power function) for each of the three aging temperatures. Then, we compute the derivative of the approximation functions (designed by Q_{50}, Q_{70} and Q_{90}). Since $\dot{Q} = (Q_\infty - Q_0)\,\dot{\xi}$, we can eliminate Q_∞ by normalizing each function $\dot{Q}_\Theta$ by $\dot{Q}_{90}$ and we obtain the normalized function: $\dot{\xi}_n(\Theta) = \dot{Q}/\dot{Q}_{90°C} = \dot{\xi}/\dot{\xi}_{90°C}$ The experimental values of $\dot{\xi}_n(\Theta)$ are obtained by calculating $\dot{Q}$ for the same value of $Q = cte$ for each aging temperature. The three experimental points allow us to determine the activation energy and the parameter m. The activation energy is determined from the slope of the line that passes through the two points defined by $\dot{\xi}_n(90°C)$ and $\dot{\xi}_n(70°C)$ considering a logarithmic scale, as illustrated in figure 17(a). Assuming that the induction temperature is fixed to $\Theta_{ind} = 320K$, the parameter m is identified by minimizing the square error between the analytical values of $\dot{\xi}_n$ (obtained from the time derivative of equation (41)) and the computed values by approximation of experimental data

$E_a(J/mol)$	m	n	$A\,C_2(s^{-1})$	Q_∞	$\Theta_{ind}(K)$
51000	32	2.746	11.69	0.658	320

Table 1: Chemical parameters

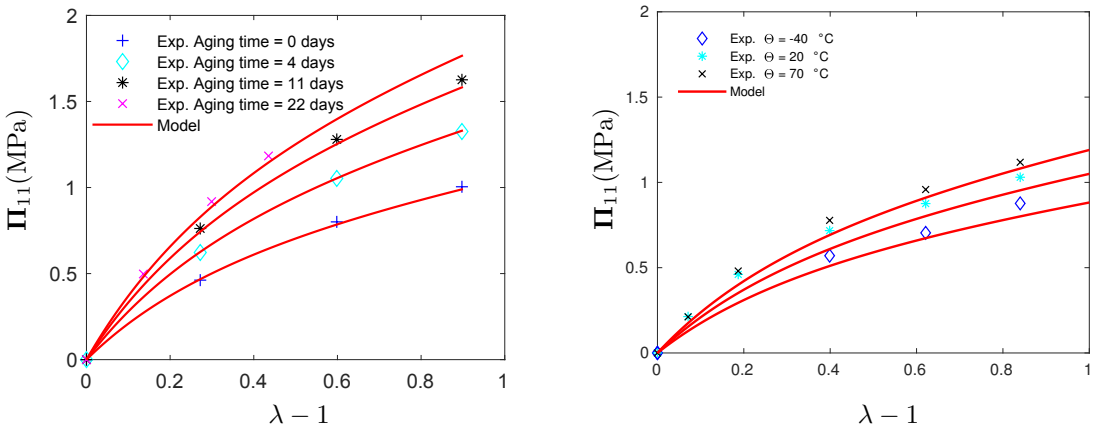

(a) Aging time dependency

(b) Temperature dependency

Figure 18: Fitting results of equilibrium responses

2. **Identification of Q_∞, n and the product $A\,C_2$**

The identification of Q_∞, n, and the product $A\,C_2$ is carried out by minimizing the square error between the experimental and analytical data of Q (eq. (42)) defined as follows:

$$Err(p_\xi) = \sum_{\Theta=50,70,90} \left(\sum_{t_i} \left[Q^{ana}\left(t_i, p_\xi\right) - Q^{exp}\left(t_i\right) \right]^2 \right) \tag{43}$$

where

- p_ξ is a chemical parameter vector: $p_\xi = \{Q_\infty, n, A\,C_2\}$
- t_i is the i^{th} aging time.

The identified parameters are gathered in table 1 and figure 17(b) shows the comparison of experimental data and model responses for different temperatures of aging.

5.2. Identification of hyperelastic parameters

To identify the hyperelastic parameters of the equilibrium contribution, we first assume the following linear form:

$$\begin{cases} C_{10}(\xi,\Theta) = C_{10}^a \xi + C_{10}^b \dfrac{\Theta - \Theta_0}{\Theta_0} + C_{10}^0 \\ C_{01}(\xi,\Theta) = C_{01}^a \xi + C_{01}^b \dfrac{\Theta - \Theta_0}{\Theta_0} + C_{01}^0 \end{cases} \tag{44}$$

where Θ_0 is the reference temperature: $\Theta_0 = 293K$. This identification is carried out as previously for the chemical part (by means of a curve-fitting algorithm employing a least-square optimization approach). We consider the minimization of the following error:

$$Err_{eq}(p) = \sum_i \left[\sigma_{eq}^{ana}\left(\lambda_i, p\right) - \sigma_{eq}^{exp}\left(\lambda_i\right) \right]^2 \tag{45}$$

$C_{10}(\xi,\Theta)\,(MPa)$	$C_{01}(\xi,\Theta)\,(MPa)$
$0.37\xi + 0.146\frac{\Theta-\Theta_0}{\Theta_0} + 0.2$	$0.32\xi + 0.175\frac{\Theta-\Theta_0}{\Theta_0} + 0.2$

Table 2: Hyperelastic parameters

where p is a parameter vector containing the hyperelastic coefficients and λ_i is the i^{th} experimental relative elongation (obtained from tests at ambient temperature after aging or on virgin specimens at different temperatures). For the temperature dependence, we used the experimental data obtained from tensile-relaxation tests performed on virgin diabolo specimens already presented in (Delattre et al., 2016). The identified parameters are gathered in table 2. Figure 18 shows the identification results of the hyperelastic parameters. Figure 18(a) shows the results of the aging time dependency part and figure 18(b) shows the results of the temperature dependency part

5.3. Identification of viscoelastic parameters

Figure 20 shows a comparison between the model and the experimental results of the evolution of the stabilized hysteresis as a function of aging temperature for aged samples during the same aging time for the same static and dynamic amplitudes (see the experimental curves in figure 11). The viscoelastic parameters are determined using an identification strategy similar to that proposed in Delattre et al. (2016). It consists of three main steps: First, a set of characteristic times (τ_1,τ_2,,..,τ_P) and Payne parameters (h_1, r_1, h_2, r_2, .., h_P, r_P), with $P > N$, are fixed a priori and supposed to be independent of both ξ and Θ. This allows us to integrate each evolution equation for each test case separately and a semi-analytical expression of the identification error can be obtained. The associated shear moduli ($\mu_1^v, \mu_2^v, .., \mu_P^v$) are assumed to be linearly dependent on ξ and Θ as follows:

$$\mu_i^v(\xi,\Theta) = \mu_i^a \xi + \mu_i^b \frac{\Theta-\Theta_0}{\Theta_0} + \mu_i^0 \quad i = 1..P \tag{46}$$

The parameters $\mu_i^a, \mu_i^b, \mu_i^0$ are identified in the second step by minimizing a relative square error defined as the sum of two relative errors. The first one corresponds to the relative error between the values of dynamic modulus obtained from the model and the experimental results. The second one corresponds to the relative error obtained from the hysteresis areas that are calculated from the model or from the experimental results.

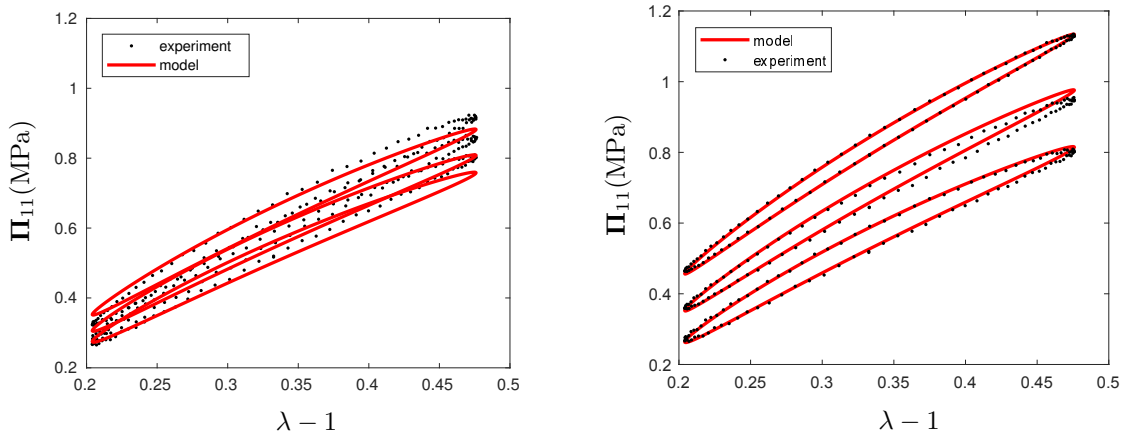

(a) Aging temperature = 70°C (b) Aging temperature = 90°C

Figure 19: Stabilized hysteresis at different aging times ($f = 10Hz$, Static amplitude = 0.34, Dynamic amplitude = 0.136)

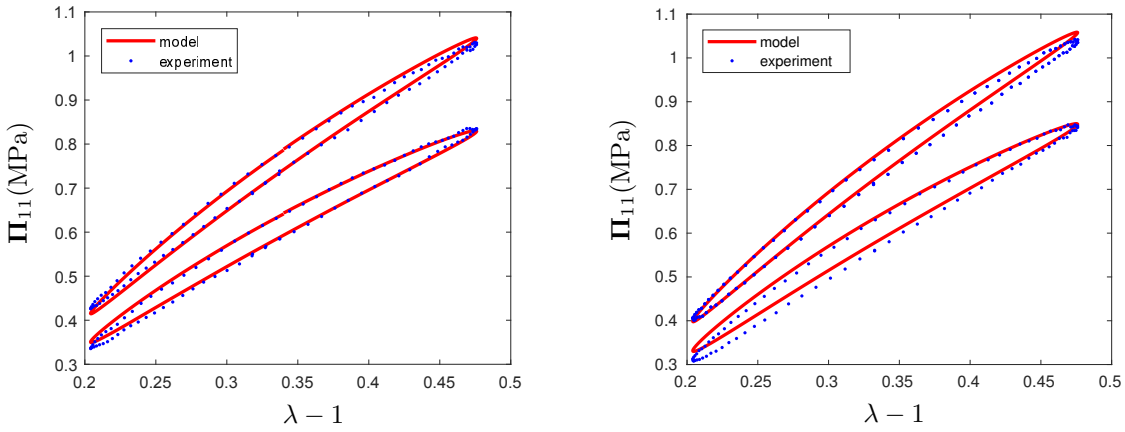

(a) $f = 3Hz$ (b) $f = 10Hz$

Figure 20: Stabilized hysteresis at different aging temperatures (Aging time = 8 *days*, Static amplitude = 0.34, Dynamic amplitude = 0.136)

The relative square error to minimize is, then, given by:

$$Err_{neq}(p_v) = \sum_{j=1}^{N_{cyclictests}} \left[\frac{R^j(p_v) - R^j_{exp}}{R^j_{exp}} \right]^2 + \sum_{j=1}^{N_{cyclictests}} \left[\frac{A^j(p_v) - A^j_{exp}}{A^j_{exp}} \right]^2 \tag{47}$$

where R^j_{exp} and R^j are respectively the experimental stiffness and the model stiffness (slope of the median of a stabilized hysteresis), A^j_{exp} and A^j denote respectively the experimental hysteresis area and the model hysteresis area (for a stabilized cycle) and $p_v = \{\mu^v_1, \mu^v_2, .., \mu^v_P\}$ is the set of shear moduli.

In order to minimize the computing time, μ^a_i, μ^b_i and μ^0_i , $i = 1..N$ are identified separately as follows:

1. Determine μ^0_i and μ^a_i, $i = 1..N$ by minimizing $Err_{neq}(\mu^a_1\xi + \mu^0_1, \mu^a_2\xi + \mu^0_2, .., \mu^a_N\xi + \mu^0_N)$ for four different values of ξ and $\Theta = \Theta_0$ simultaneously.
2. Determine μ^b_i, $i = 1..N$ by minimizing $Err_{neq}(\mu^b_1 \frac{\Theta-\Theta_0}{\Theta_0} + \mu^0_1, \mu^b_2 \frac{\Theta-\Theta_0}{\Theta_0} + \mu^0_2, .., \mu^b_N \frac{\Theta-\Theta_0}{\Theta_0} + \mu^0_N)$ at $\xi = 0$ and for the two other values of Θ simultaneously.

The arbitrary set of characteristic times and Payne parameters is eventually redefined in a third step to keep only the parameters that contribute significantly to the error defined at eq. (47). Insignificant characteristic times are therefore eliminated. This procedure allows us to let the minimization process determine the number, N, of characteristic times that are needed to represent the behavior. The identified parameters are gathered in table 3.

Figure 19 depicts a comparison between the model and the experimental results of the evolution of stabilized hysteresis as a function of the aging time for two different aging temperatures (70°C figure 19(a)) and 90°C (figure 19(b)) at the same frequency, static amplitude and dynamic amplitude (see the experimental curves in figure 8).

Figure 21 depicts a comparison between the model and the experimental results of the evolution of the stabilized hysteresis as a function of frequency for the same static and dynamic amplitudes. The model describes well the frequency dependency. Figure 22 shows a comparison between the model and the experimental results of the evolution of the stabilized hysteresis as a function of static and dynamic amplitudes four different aging times. It shows that the Payne effect is well captured by the model.

We can also compare the results obtained from the model for full relaxation tests that are not used in the identification procedure (only the equilibrium stress is used for the equilibrium part of the model). The results are shown in figure 23 for two aging temperatures: 70°C and 90°C.

The previous figures show that all the experimental dynamic observations are quite well described by the model.

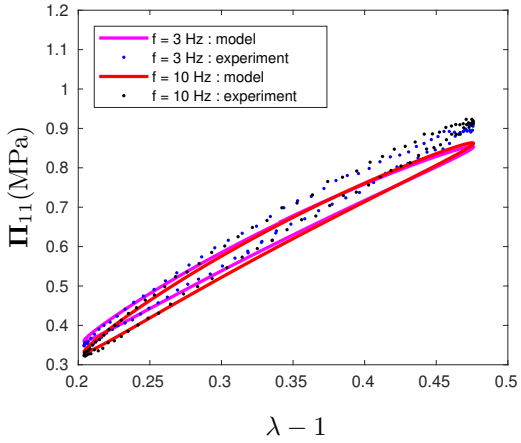

(a) Aging temperature = 70°C, Aging time = 12 *days*

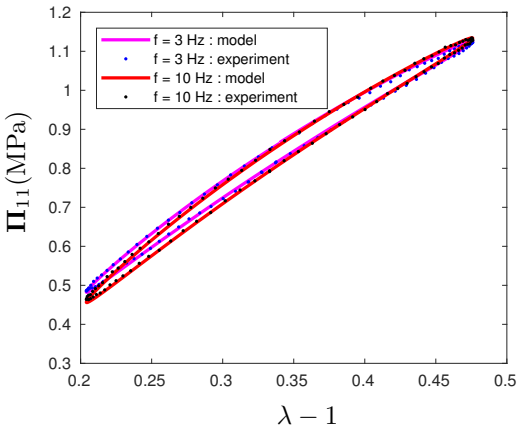

(b) Aging temperature = 90°C, Aging time = 11 *days*

Figure 21: Stabilized hysteresis at two different frequencies (Static amplitude = 0.34, Dynamic amplitude = 0.136)

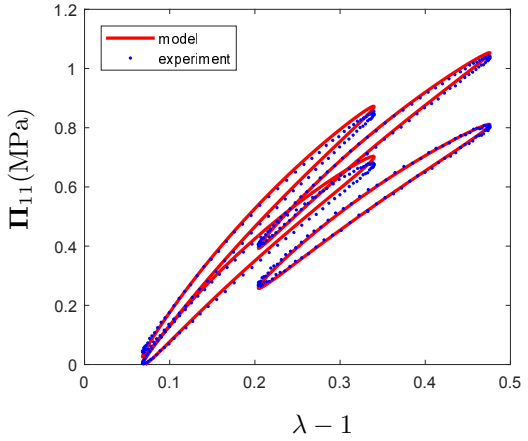

(a) Dynamic amplitude = 0.136, Aging time = 8 *days*

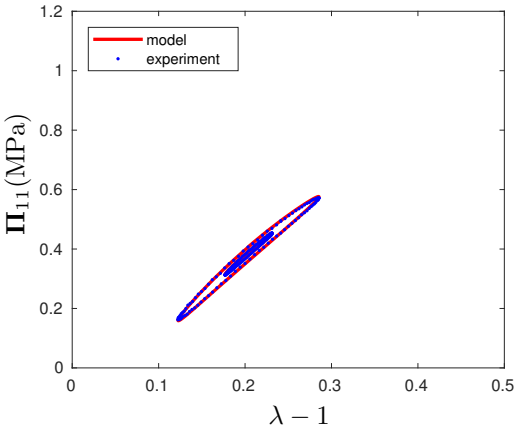

(b) Static amplitude = 0.34, Aging time = 0 *days*

Figure 22: Stabilized hysteresis at different static and dynamic amplitudes ($f = 10Hz$, Aging temperature = 90°C)

$\tau_i\,(s)$	$h_i\,(s)$	r_i	$\mu_i(\xi,\Theta)\,(MPa)$
0.01	1	0.05	$-0.0365\xi - 0.0586\frac{\Theta-\Theta_0}{\Theta_0} + 0.1167$
0.01	1	5	-0.0448ξ
0.1	1	0.05	$-0.0016\xi + 0.0836$
0.1	1	5	-0.0499ξ
1	1	0.05	$-0.0039\xi - 0.3811\frac{\Theta-\Theta_0}{\Theta_0} + 0.0110$
1	1	5	-0.0119ξ
10	1	0.05	$-0.0586\frac{\Theta-\Theta_0}{\Theta_0} + 0.1415$
10	1	5	$-0.1759\frac{\Theta-\Theta_0}{\Theta_0}$

Table 3: Viscoelastic parameters

6. Finite element simulation

6.1. Variational formulation and numerical implementation

In the following we consider the case of heterogeneous and non isothermal aging. The equilibrium equations of the thermo-mechanical state can be written in the reference configuration (considering only the

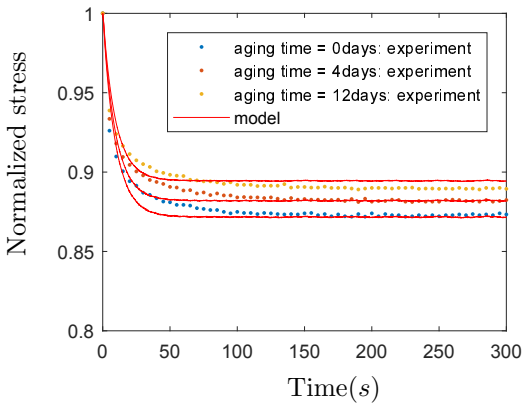

(a) Relaxation curves for samples aged at 70°C

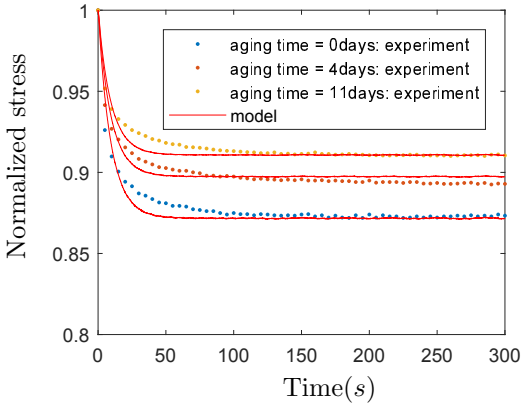

(b) Relaxation curves for samples aged at 90°C

Figure 23: Relaxation curves at 10mm of displacement ($\lambda = 1.272$) for different aging times

quasi-static case):

$$\begin{aligned}
&\mathrm{DIV}_{\mathbf{X}}\boldsymbol{\Pi} + \rho_0\mathbf{f} = \mathbf{0} \quad \forall \mathbf{X} \in \Omega_0 \\
&\rho_0 C_p \dot{\Theta} = J\sum_{i=1}^{N}\phi^i_{vis} + J\sum_{i=1}^{N}\phi^i_{payne} + J\phi_\xi + \rho_0 r + Jl_m + Jl_q + Jl_\xi - \mathrm{DIV}_{\mathbf{X}}\mathbf{Q}_\Theta \quad \forall \mathbf{X} \in \Omega_0
\end{aligned} \tag{48}$$

where Ω_0 is the body in the initial configuration, $\mathrm{DIV}_{\mathbf{X}}$ is the Lagrangian divergence operator, $\mathbf{Q}_\Theta = J\mathbf{q}_\Theta\mathbf{F}^{-\mathrm{T}}$ is the heat flux in the reference configuration, $\mathbf{f}$ is the current body force expressed per unit of undeformed volume, $\boldsymbol{\Pi} = J\boldsymbol{\sigma}\mathbf{F}^{-\mathrm{T}}$ is the first Piola-Kirchoff stress. Equations (48) must be completed with appropriate initial and boundary conditions:

$$\begin{aligned}
&\Theta(t=0) = \Theta_0 \quad \text{in} \quad \Omega_0 \\
&\Theta = \theta \quad \text{on} \quad \partial\Omega_\Theta \quad \mathbf{Q}_\Theta\mathbf{N}dS = Q_0 \quad \text{on} \quad \partial\Omega_Q \\
&\mathbf{u} = \mathbf{u}_0 \quad \text{on} \quad \partial\Omega_{\mathbf{u}} \quad \boldsymbol{\Pi}\mathbf{N}dS = \mathbf{T} \quad \text{on} \quad \partial\Omega_f
\end{aligned} \tag{49}$$

These equilibrium equations are fully coupled and need to be complemented with the previous set of constitutive and evolution equations. In order to take into consideration the nearly-incompressibility constraint and fully thermo-chemo-mechanical coupling, we propose to adopt the following variational formulation that corresponds to the weak form of the local eqs. (48), (49), (29), (37):

$$\begin{aligned}
&\mathrm{Find}(\mathbf{u}, q, \Theta, \xi), \quad \text{such that } \forall(\delta\mathbf{u}, \delta q, \delta\Theta, \delta\xi) \\
&\int_{\Omega_0}\left(\boldsymbol{\Pi}^{DEV}_{eq} + \sum_{i=1}^{N}\boldsymbol{\Pi}^i_v + q\frac{J}{J_\Theta}\mathbf{F}^{-\mathrm{T}}\right) : \mathbf{F}(\delta\mathbf{u})d\Omega_0 - \int_{\Omega_0}\rho_0\mathbf{f}\delta\mathbf{u}d\Omega_0 - \int_{\partial\Omega_f}\mathbf{T}\delta\mathbf{u}dS = 0 \\
&\int_{\Omega_0}\rho_0 C_p\dot{\Theta}\delta\Theta d\Omega_0 - \int_{\Omega_0}\left(J\sum_{i=1}^{N}\phi^i_{vis} + J\sum_{i=1}^{N}\phi^i_{payne} + J\phi_\xi + \rho_0 r + Jl_m + Jl_q + Jl_\xi\right)\delta\Theta d\Omega_0 \\
&\quad - \int_{\Omega_0}\mathbf{Q}_\Theta\mathrm{GRAD}_{\mathbf{X}}\delta\Theta d\Omega_0 + \int_{\partial\Omega_Q}\mathbf{Q}_0\delta\Theta dS = 0 \\
&\int_{\Omega_0}\left(\frac{J}{J_\Theta} - \exp\left(\frac{q}{k}\right)\right)\delta q d\Omega_0 = 0 \\
&\int_{\Omega_0}\left(\dot{\xi} - k_\xi(\Theta)\left\langle A_\xi\right\rangle\right)\delta\xi d\Omega_0 = 0
\end{aligned} \tag{50}$$

where $\mathbf{\Pi}_{eq}^{DEV} = J\boldsymbol{\sigma}_{eq}^{\mathrm{D}}\mathbf{F}^{-T}$ and $\mathbf{\Pi}_{v}^{i} = J\boldsymbol{\sigma}_{v}^{i}\mathbf{F}^{-T}$. We consider a backward Euler scheme to integrate the previous system with respect to time. The time step is defined as $\Delta t = (t_n, t_{n+1})$. All the quantities are known at time t_n and are unknown at time t_{n+1}. The previous system of equations becomes:

$$
\begin{aligned}
&\text{Find}(\mathbf{u}^{n+1}, q^{n+1}, \Theta^{n+1}, \xi^{n+1}), \quad \text{such that } \forall(\delta\mathbf{u}, \delta q, \delta\Theta, \delta\xi)\\
&\int_{\Omega_0} (\mathbf{\Pi}_{eq}^{DEV^{n+1}} + \sum_{i=1}^{N} \mathbf{\Pi}_{v}^{i^{n+1}} + q^{n+1}\frac{J^{n+1}}{J_{\Theta}^{n+1}}\mathbf{F}^{-\mathrm{T}^{\mathbf{n+1}}}) : \mathbf{F}(\delta\mathbf{u})d\Omega_0 - \int_{\Omega_0} \rho_0\mathbf{f}^{n+1}\delta\mathbf{u}d\Omega_0 - \int_{\partial\Omega_f} \mathbf{T}^{n+1}\delta\mathbf{u}dS = 0\\
&\int_{\Omega_0} \rho_0\frac{C_p^{n+1}}{\Delta t}(\Theta^{n+1} - \Theta^n)\delta\Theta d\Omega_0 - \int_{\Omega_0} \Bigg(J^{n+1}\sum_{i=1}^{N}\phi_{vis}^{i^{n+1}} + J^{n+1}\sum_{i=1}^{N}\phi_{payne}^{i^{n+1}} + J^{n+1}\phi_{\xi}^{n+1} + \rho_0 r^{n+1}\\
&\quad + J^{n+1}l_m^{n+1} + J^{n+1}l_q^{n+1} + J^{n+1}l_{\xi}^{n+1}\Bigg)\delta\Theta d\Omega_0 - \int_{\Omega_0} \mathbf{Q}_{\Theta}^{n+1}\mathrm{GRAD}_{\mathbf{X}}\delta\Theta d\Omega_0 + \int_{\partial\Omega_Q} \mathbf{Q}_0^{n+1}\delta\Theta dS = 0\\
&\int_{\Omega_0} \left(\frac{J^{n+1}}{J_{\Theta}^{n+1}} - \exp\left(\frac{q^{n+1}}{k}\right)\right)\delta q d\Omega_0 = 0\\
&\int_{\Omega_0} \left(\frac{\xi^{n+1} - \xi^n}{\Delta t} - k_{\xi}(\Theta^{n+1})\left\langle A_{\xi}^{n+1}\right\rangle\right)\delta\xi d\Omega_0 = 0
\end{aligned}
\tag{51}
$$

The space discretization of the previous system of equations can be done with a standard Galerkine procedure. We use a finite element approximation for each field of this formulation. The previous non-linear system of equation is linearized and a Newton-Raphson scheme is used to solve it incrementally. It can be noticed that, first, the set of equations (51) leads to a non-symmetric linear operator (tangent matrix) and second, within the hybrid free energy formulation there is no need to consider a specific variational principle, the link between the thermodynamics and the variational formulation being straightforward even for nearly incompressible behaviors (i.e. $k \to \infty$).

The constitutive equations are considered at Gauss points of each finite element, the evolution equations for viscosity (33) or for Payne (35) are integrated locally at each Gauss point with substepping backward Euler schemes (e.g. Lejeunes et al. (2011)). We integrated all these developments within the simulation platform FEMJava that is being developed in our laboratory.

6.2. Creep aging test: identification of the chemo-mechanical coupling

To study the influence of a permanent stress during aging, we realized a creep aging test on tensile specimens (H2 specimen). Specimens were clamped one side and a mass of $300g$ was suspended on the opposite side (see figure 24(a)). Loaded specimens were then put in a oven (without air flow) for 25 days at 70^oC. Some specimens were periodically removed from the oven and unloaded. After complete stress and thermal relaxation, we proceeded with swelling tests in two distinct areas of each specimen: in the central zone that was stretched during creep and in the head of the specimen where the stretch was negligible during creep. Figure 24(b) shows that there is a gradient of maturation of the cross-link network that is correlated to the stress state: in the central area the chemo-physical evolution is smaller than in the head of the specimen.

To simulate this test, we consider the following model: tensile H2 specimen geometry is meshed in 3D with quadratic hexahedral elements. We chose $U2P1^0T2C2$ (quadratic for the displacement field, linear and discontinuous between elements for the pressure field, quadratic for the temperature field and quadratic ξ field) interpolation for the unknown fields in the hexahedral elements. We assume adiabatic conditions on the boundaries, one side is fixed (all kinematic boundaries are null) and we apply a constant load onto the other side (the nodes of this side are tied so as to behave as a rigid body). Mechanical loading starts to be applied at the initial temperature (20^oC). The material parameters not already defined in the previous section are given in table 4. The entire body is heated through the volumetric term $\rho_0 r$ so as to reach a homogeneous temperature of 70^oC in the specimen (see figure 25). The time dependence of the external heat power and the applied load is shown in figure 25(b). These boundary conditions are clearly not equivalent

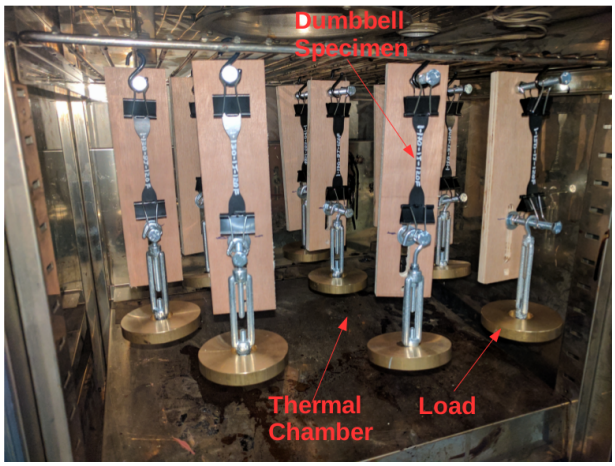

(a) experimental setup

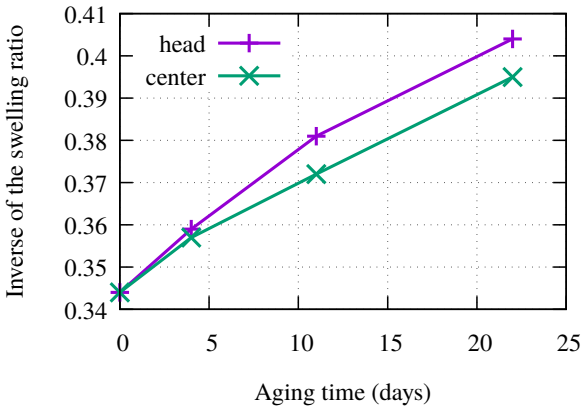

(b) evolution of the inverse of the swelling ratio as a function of aging time for two distinct zones of tensile specimens after creep

Figure 24: Creep aging test: influence of a permanent stress during aging

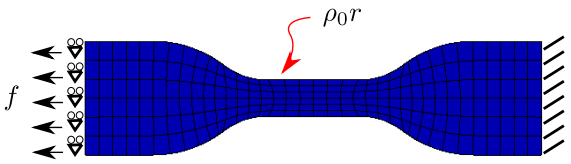

(a) mesh with quadratic hexahedral elements

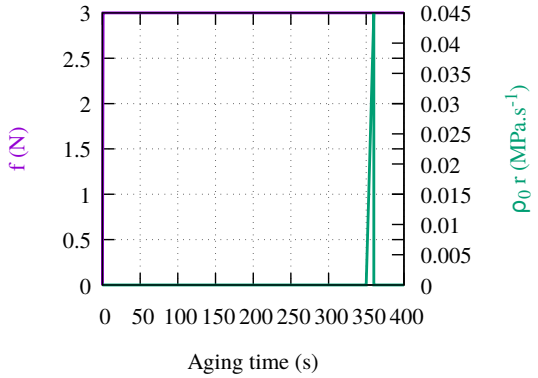

(b) load signal for the first seconds (total duration 1.7e6 s)

Figure 25: Boundary conditions and mesh for the creep aging test

$k(MPa)$	$\alpha_\Theta(K^{-1})$	$C_0(Nmm^{-2}K^{-1})$	$C_1(Nmm^{-2}K^{-1})$	$k_\Theta(Ns^{-1}K^{-1})$
1400	$6.e-4$	4.6	0.39	0.22

Table 4: Supplementary material parameters

to what is imposed in the experiments but they allow to reach an homogeneous temperature state after imposing the mechanical load, as can be seen in figure 26(a) (therefore, this is an indirect way of controlling the specimen temperature, as it is done experimentally by the thermal regulation in the oven).

Knowing the product AC_2, we can identify independently C_2 and A such that we can reproduce the experimental data of figure (24(b)). It can be seen from figures 26 that, as expected, a uniform field of temperature superimposed with a non-uniform field of stress leads to a non uniform field of relative new cross-link density. If we take from this result the nodal values of ξ at two different locations (head and central area of the specimen) we obtain the result of figure 27 for different values of C_2. It can be seen that we can fit experimental results with a relative good agreement for $C_2 = 1.43\,MPa$. It can also be noticed

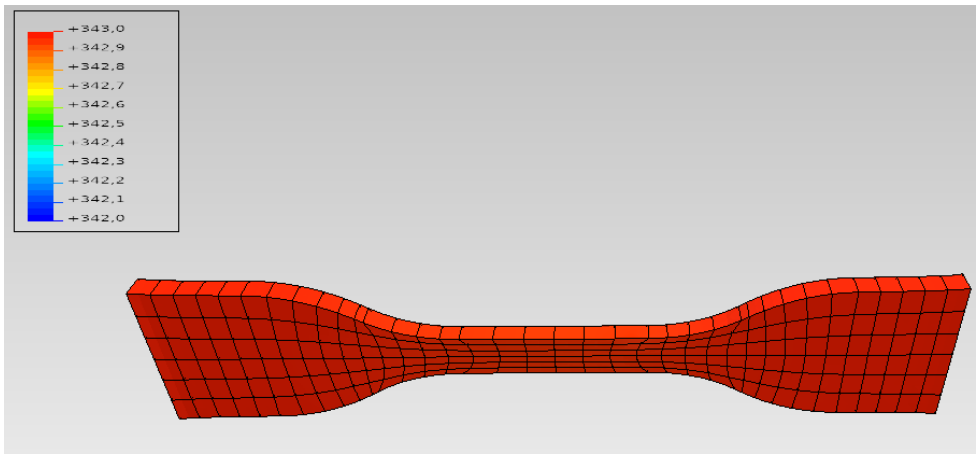

(a) Temperature field in Kelvin at the end of the heating and mechanical loading phase

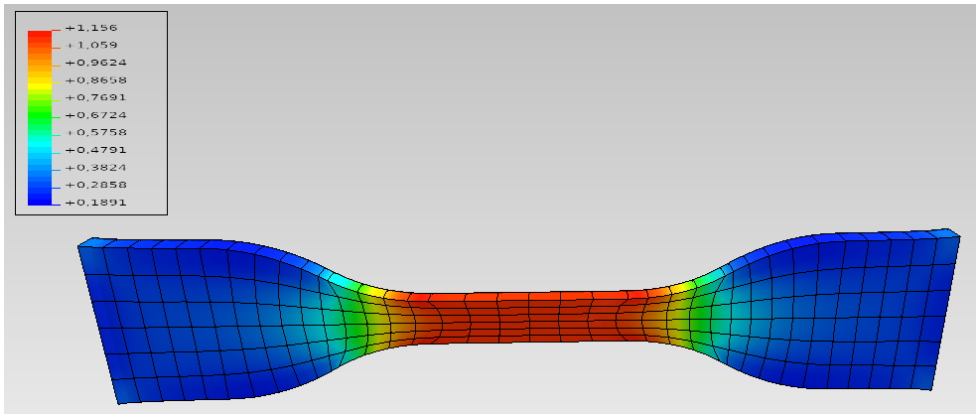

(b) Axial stress field (Cauchy stress in MPa) at the end of the heating and mechanical loading phase

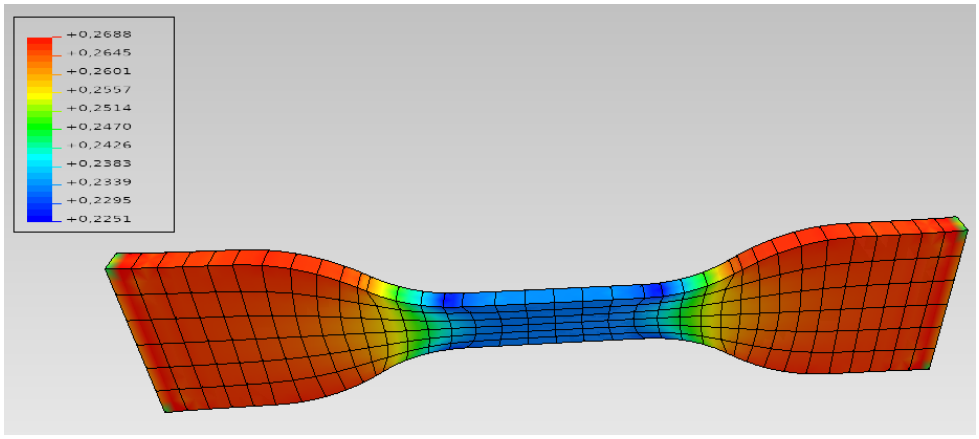

(c) Chemical conversion field after 22 aging days

Figure 26: FE simulation results of the numerical creep aging test (for $C_2 = 1.43\,MPa$ and $A = 8.17 MPa^{-1}s^{-1}$)

that, as expected, the impact of the mechanical loading on the chemical evolution decreases if C_2 increases.

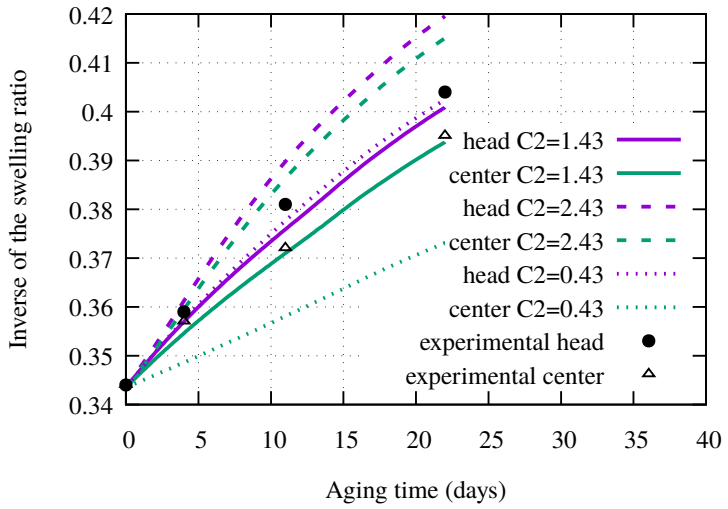

Figure 27: Comparison of numerical simulation and experimental results for the thermal creep aging test

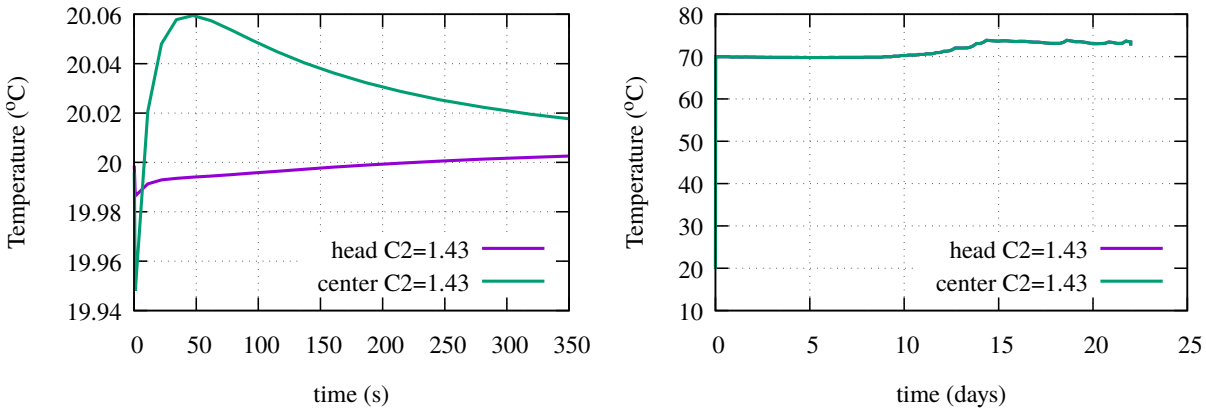

(a) during creep at ambient temperature

(b) during thermal aging with creep

Figure 28: Evolution of the temperature upon time from the numerical FE simulation

Taking a value of $C_2 = 1.43\,MPa$, we can also represent the evolution of the temperature and the Cauchy stress at the same FE nodes as for ξ in figures 28 and 29. From the temperature evolution, we can see in the very first seconds the thermal inversion phenomena (decrease and increase in the temperature due to a competition between thermal dilation and entropic elasticity) during the mechanical loading. During the creep phase (constant force at ambient temperature) the temperature decreases in the central zone due to viscous phenomena (thermal softening effect) while it continues to increase in the head area where viscosity is not playing a role. During the heating and aging phase (after creep) the temperature is homogeneous and it slightly increases due to adiabatic boundary conditions and dissipation due to chemical processes (which are exothermic). From the stress and displacement results, we can see that during the aging phase the Cauchy stress in the central zone is relaxed while nearly constant in the head zone. This can be due to a combination of factors: first the entropic elasticity (increasing temperature leads to contraction), second the non homogeneous cross-link density evolution (structural effect) and third the thermal dilatation (the cross section varies while the applied force is constant). This test illustrates the strong thermo-chemo-mechanical

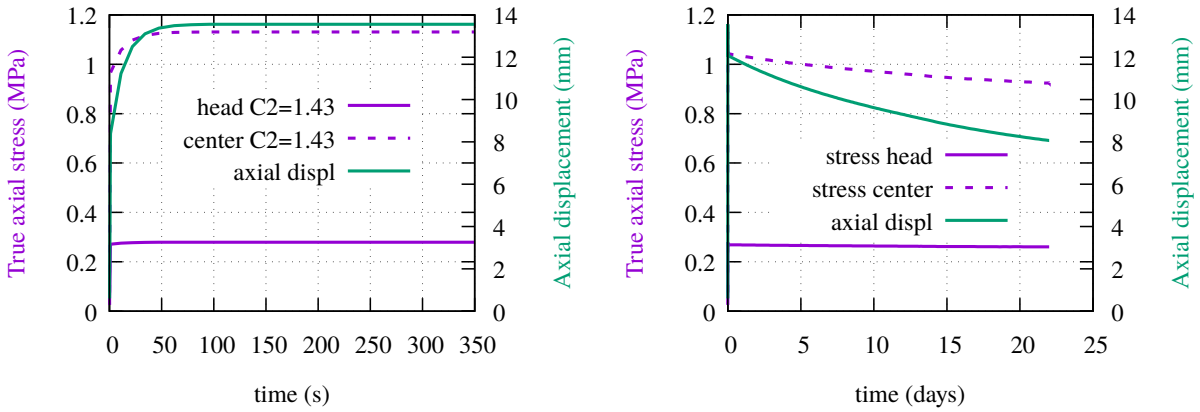

(a) during creep at ambient temperature

(b) during thermal aging with creep

Figure 29: Cauchy stress and global displacement results from the numerical FE simulation

coupling effects that can be taken into account with this model.

7. Conclusion

We have proposed a new constitutive model that is based on a strong thermo-chemo-mechanical coupling approach to predict the (thermo-mechanical) behavior of filled rubber subjected to thermal aging phenomena. It takes into account the consequence of aging on the mechanical properties including specific dynamic nonlinearities such as the Payne effect or the self heating phenomenon. In accordance with the experimental observations that are presented in this paper, the thermal aging is modelized considering only anaerobic chemical crosslink maturation processes (polysulfidic to mono or di-sulfidic crosslinks). The influence of a non-free stress state during thermal aging and the non-Arrhenius behavior for the thermal kinetic term are two of the main original contributions of this modeling approach. The hybrid energy concept (Lejeunes and Eyheramendy (2018)) that is used in this work allows us to obtain a straightforward fully coupled variational formulation. This variational formulation is consistent with the constitutive equations obtained from the thermodynamics formulation and allows to account for nearly-incompressible behavior without making use of Lagrange multipliers or other specific variational principles. It can also be used to couple the chemo-physical evolution law with the hydrostatic pressure if needed. The identification of the material parameters can be mainly made with the help of mechanical tests (before and after aging) coupled to swelling tests. The chemo-mechanical coupling contribution is fully identified with the help of finite element simulations of a creep aging test, which leads to a heterogeneous level of aging due the heterogeneous stress field. This model is a first step for describing more complex situations where chemo-physical network evolution can occur in filled rubber (for instance when submitted to cyclic thermo-mechanical loading). It will help us to define more complicated experiments for validation or new developments.

8. Acknowledgments

The project leading to this publication has received funding from the Labex MEC (Mechanics and Complexity) an Excellence Initiative of Aix-Marseille University - A*MIDEX, a French “Investissements d’Avenir” program.

References

Budrugeac, P., 1995. Accelerated thermal ageing of nitrile-butadiene rubber under air pressure. Polymer Degradation and Stability 47 (1), 129 – 132.
URL http://www.sciencedirect.com/science/article/pii/014139109400101D

Choi, S., Jose, J., Lyu, M., Huh, Y., Cho, B. H., Nah, C., December 2010. Influence of filler and cure systems on thermal aging resistance of natural rubber vulcanizates under strained condition. Journal of Applied Polymer Science 118 (5), 3074–3081.

Choi, S.-S., Kim, J.-C., 2012. Lifetime prediction and thermal aging behaviors of sbr and nbr composites using crosslink density changes. Journal of Industrial and Engineering Chemistry 18 (3), 1166 – 1170.
URL http://www.sciencedirect.com/science/article/pii/S1226086X12000160

Delattre, A., Lejeunes, S., Lacroix, F., Méo, S., 2016. On the dynamical behavior of filled rubbers at different temperatures : Experimental characterization and constitutive modeling. International Journal of Solids and Structures 90, 178–193.

Delattre, A., Lejeunes, S., Méo, S., Lacroix, F., Richard, C., 2014. On the multiaxial amplitude and frequency dependent behavior of rubber: experiments and constitutive modeling. Rubber Chemistry and Technology 87 (3), 557–578.
URL https://hal.archives-ouvertes.fr/hal-01057026

Flory, J., 1953. Principles of polymer chemistry. Cornell University Press.

Flory, P. J., Rehner, J., 1943. Statistical mechanics of cross-linked polymer networks ii. swelling. The Journal of Chemical Physics 11 (11), 521–526.
URL https://doi.org/10.1063/1.1723792

Flory, R. J., 1961. Thermodynamic relations for highly elastic materials. Transactions of the Faraday Society 57, 829–838.

Gac, P. L., Saux, V. L., Paris, M., Marco, Y., 2012. Ageing mechanism and mechanical degradation behaviour of polychloroprene rubber in a marine environment: Comparison of accelerated ageing and long term exposure. Polymer Degradation and Stability 97 (3), 288 – 296.
URL http://www.sciencedirect.com/science/article/pii/S0141391011004149

Germain, P., Nguyen, Q., Suquet, P., 1983. Continuum thermodynamics. Journal of Applied Mechanics 50, 1010–1020.
URL http://dx.doi.org/10.1115/1.3167184

Gigliotti, M., Grandidier, J.-C., 2010. Chemo-mechanics couplings in polymer matrix materials exposed to thermo-oxidative environments. Comptes Rendus Mécanique 338 (3), 164 – 175.
URL http://www.sciencedirect.com/science/article/pii/S1631072110000240

Gigliotti, M., Grandidier, J.-C., Lafarie-Frenot, M. C., 2011. Assessment of chemo-mechanical couplings in polymer matrix materials exposed to thermo-oxidative environments at high temperatures and under tensile loadings. Mechanics of Materials 43 (8), 431 – 443.
URL http://www.sciencedirect.com/science/article/pii/S016766361100069X

Gigliotti, M., Minervino, M., Lafarie-Frenot, M., Grandidier, J., 2016. Effect of thermo-oxidation on the local mechanical behaviour of epoxy polymer materials for high temperature applications. Mechanics of Materials 101, 118 – 135.
URL http://www.sciencedirect.com/science/article/pii/S0167663616301508

Johlitz, M., Diercks, N., Lion, A., 2014. Thermo-oxidative ageing of elastomers: A modelling approach based on a finite strain theory. International Journal of Plasticity 63, 138 – 151, deformation Tensors in Material Modeling in Honor of Prof. Otto T. Bruhns.
URL http://www.sciencedirect.com/science/article/pii/S0749641914000692

Johlitz, M., Lion, A., 2013. Chemo-thermomechanical ageing of elastomers based on multiphase continuum mechanics. Continuum Mechanics and Thermodynamics 25 (5), 605–624.

Kari, L., Sep 2017. Dynamic stiffness of chemically and physically ageing rubber vibration isolators in the audible frequency range. Continuum Mechanics and Thermodynamics 29 (5), 1027–1046.
URL https://doi.org/10.1007/s00161-017-0569-7

Kraus, G., Childers, C. W., Rollmann, K. W., 1966. Stress softening in carbon black reinforced vulcanizates. strain rate and temperature effects. Rubber Chemistry and Technology 39 (5), 1530–1543.
URL http://dx.doi.org/10.5254/1.3547068

Lejeunes, S., Boukamel, A., Méo, S., 2011. Finite element implementation of nearly-incompressible rheological models based on multiplicative decompositions. Computers & Structures 89 (3), 411 – 421.
URL http://www.sciencedirect.com/science/article/pii/S0045794910002798

Lejeunes, S., Eyheramendy, D., May 2018. Hybrid free energy approach for nearly incompressible behaviors at finite strain. Continuum Mechanics and Thermodynamics.
URL https://doi.org/10.1007/s00161-018-0680-4

Lejeunes, S., Eyheramendy, D., Boukamel, A., Delattre, A., Méo, S., Ahose, K. D., Feb 2018. A constitutive multiphysics modeling for nearly incompressible dissipative materials: application to thermo–chemo-mechanical aging of rubbers. Mechanics of Time-Dependent Materials 22 (1), 51–66.
URL https://doi.org/10.1007/s11043-017-9351-2

Lion, A., 1996. A constitutive model for carbon black filled rubber: Experimental investigations and mathematical representation. Continuum Mechanics and Thermodynamics 8 (3), 153–169.
URL http://dx.doi.org/10.1007/BF01181853

Lion, A., Dippel, B., Liebl, C., 2014. Thermomechanical material modelling based on a hybrid free energy density depending on pressure, isochoric deformation and temperature. International Journal of Solids and Structures 51 (3–4), 729 – 739.
URL http://www.sciencedirect.com/science/article/pii/S0020768313004319

Lion, A., Johlitz, M., 2012. On the representation of chemical ageing of rubber in continuum mechanics. International Journal of Solids and Structures 49 (10), 1227 – 1240.
URL http://www.sciencedirect.com/science/article/pii/S0020768312000303

Minervino, M., Gigliotti, M., Lafarie-Frenot, M., Grandidier, J., 2014. A coupled experimental/numerical approach for the modelling of the local mechanical behaviour of epoxy polymer materials. Journal of the Mechanics and Physics of Solids 67, 129 – 151.

URL http://www.sciencedirect.com/science/article/pii/S0022509614000398

Mousa, A., Ishiaku, U. S., Ishak, Z. A. M., 2002. Thermo-oxidative aging and fatigue behavior of dynamically vulcanized pvc/enr thermoplastic elastomers. International Journal of Polymeric Materials and Polymeric Biomaterials 51 (11), 967–980.
URL https://doi.org/10.1080/714975687

Musil, B., Johlitz, M., Lion, A., Oct 2018. On the ageing behaviour of nbr: chemomechanical experiments, modelling and simulation of tension set. Continuum Mechanics and Thermodynamics.
URL https://doi.org/10.1007/s00161-018-0728-5

N'Guyen, T., Lejeunes, S., Eyheramendy, D., Boukamel, A., 2016. A thermodynamical framework for the thermo-chemo-mechanical couplings in soft materials at finite strain. Mechanics of Materials 95, 158 – 171.
URL http://www.sciencedirect.com/science/article/pii/S016766361600017X

Pimolsiriphol, V., Saeoui, P., Sirisinha, C., 2007. Relationship among thermal ageing degradation, dynamic properties, cure systems, and antioxidants in natural rubber vulcanisates. Polymer-Plastics Technology and Engineering 46 (2), 113–121.
URL https://doi.org/10.1080/03602550601152861

Rabanizada, N., Lupberger, F., Johlitz, M., Lion, A., Aug 2015. Experimental investigation of the dynamic mechanical behaviour of chemically aged elastomers. Archive of Applied Mechanics 85 (8), 1011–1023.
URL https://doi.org/10.1007/s00419-014-0971-6

Tomer, N., Delor-Jestin, F., Singh, R., Lacoste, J., 2007. Cross-linking assessment after accelerated ageing of ethylene propylene diene monomer rubber. Polymer Degradation and Stability 92 (3), 457 – 463.
URL http://www.sciencedirect.com/science/article/pii/S0141391006003260

Treloar, L. R. G., 1943. The elasticity of a network of long-chain molecules. Transactions of the Faraday Society 39, 36–41.

Ulmer, J. D., 1996. Strain dependence of dynamic mechanical properties of carbon black-filled rubber compounds. Rubber Chemistry and Technology 69 (1), 15–47.
URL http://dx.doi.org/10.5254/1.3538354